

# Chapter 4

## Experimental set-ups

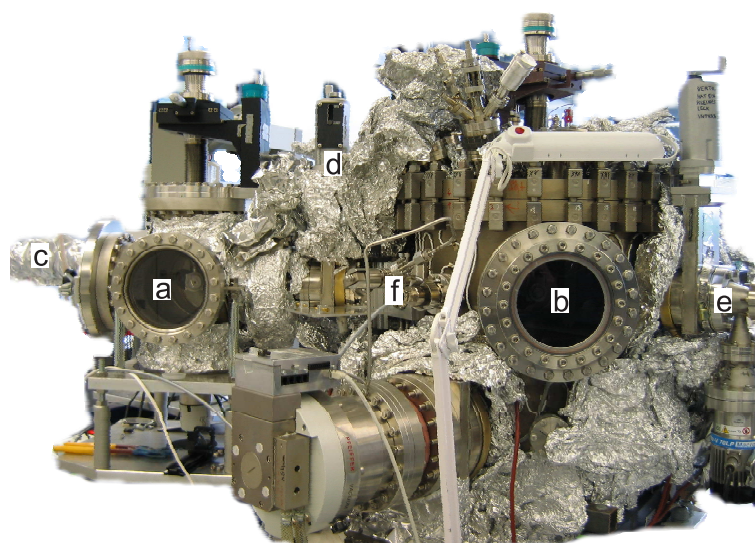
This chapter is devoted to the description of the experimental set-ups used in this thesis. In the first section, the in-house UHV system used for the preparation and characterization of the sample surface prior to diffraction experiments is presented. The subsequent sections comprise a brief description of the different synchrotron light sources, experimental end-stations and set-ups employed during the performance of the SXRD and HRCLS measurements.

### 4.1 Sample preparation

#### UHV chamber

The in-house UHV system shown in the Fig. 4.1 consists of two chambers (a, b) separated by a gate valve (d). The pressure is maintained in the ultra high vacuum regime by a combination of turbo molecular and ion getter pumps. Baking the chamber at 150°C for about 48 hours ensures a base pressure of  $2 \times 10^{-10}$  mbar.

The sample is first introduced in the pre-chamber (a), thereby avoiding to vent the analysis chamber (b) whenever a new sample is introduced. A horizontal manipulator allows the sample to be transferred between the introduction and analysis chamber. Inside the analysis chamber, the sample is fixed on a vertical manipulator which allows for  $x$ ,  $y$  and  $z$  translations, as well as for the rotation of the sample carousel around its axis. The analysis chamber is equipped with a gas inlet system and various standard surface science characterization tools. For this thesis, mainly the combined LEED/AES system and the ion sputter gun (f) facilities have been used. The typical sample preparation procedure involves a number of steps in order to obtain a well defined surface under reproducible conditions. The surface contaminants may be removed either by oxidation-annealing cycles or by Ar<sup>+</sup>-ion sputtering. The analysis chamber is equipped with a commercial ion



**a** Introduction chamber      **d** Gate valve between **a** and **b**  
**b** Analysis chamber        **e** Gate valve to portable UHV chamber  
**c** Transfer rod                **f** Sputter gun

**Figure 4.1:** UHV chamber for sample preparation.

source IQE 11/35 manufactured by SPECS<sup>1</sup>. A gas inlet flange allows for a direct transfer of the argon gas into the ionization cylinder cap, which results in a low operation pressure of  $10^{-6}$  to  $10^{-5}$  mbar within the main chamber. The argon is ionized in the sputter gun and accelerated at about 1 keV onto the sample surface.

A free port is available for connecting the portable UHV diffraction chamber. This is separated from the analysis chamber by the gate valve (e) and a second horizontal manipulator (c) is available for transferring the sample directly into the portable UHV chamber, which is then shipped to the synchrotron facility for performance of the diffraction experiments.

## LEED/AES system

The analysis chamber is equipped with a combined LEED/AES system, shown in Fig. 4.2, which allows for the characterization of the sample surface. It is a commercial system, ErLEED 150, manufactured by SPECS GmbH. The filament emits electrons onto the sample, where they are backscattered. In the directions of constructive interference, intensity maxima will be detected on the fluorescent screen. A number of grids (shown in the right panel of Fig. 4.2) are placed between the sample and the screen to make sure that only elastically scattered electrons are detected and that the directions of the electrons will not be affected by any electric fields. The reverse view optics and the transparent

<sup>1</sup>SPECS GmbH - Surface Analysis and Computer Technology, Berlin, Germany; <http://www.specs.de>.

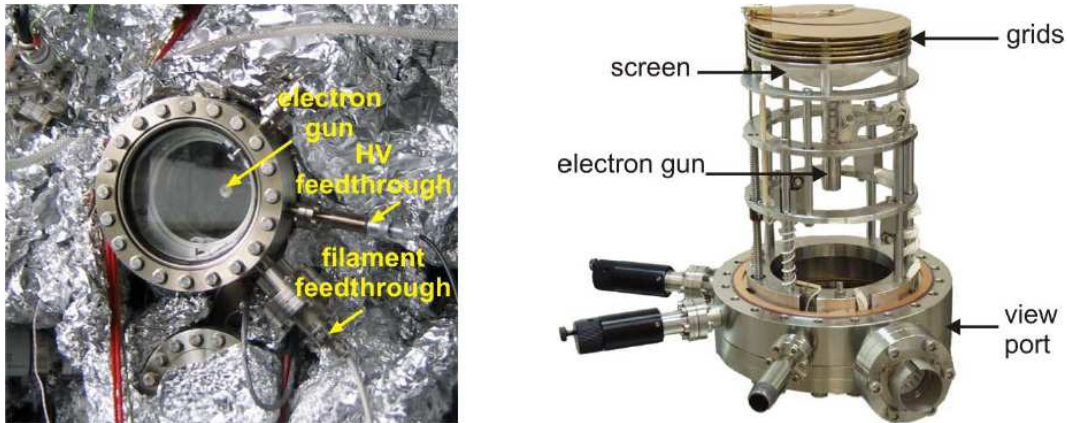


**Figure 4.2:** The LEED/AES system used for sample preparation.

fluorescent screen makes it possible to observe the diffraction pattern at the position of the LEED flange (shown in the left panel of Fig. 4.2). The LEED optics can also be used as an electron energy analyzer or, more precisely, a RFA which offers the possibility of recording Auger electron spectra. The system is operated with a ErLEED 3000 control unit which has an integrated Lock-In amplifier (for AES) and can control the HV on several modules (i.e., the anode, the grids, the screen, the collector). The primary energy can be varied between 0–1000 eV and 0–3000 eV when operated in the LEED and AES mode, respectively. More detailed technical information on the ErLEED system can be found on the SPECS GmbH web site ([www.specs.de](http://www.specs.de)).

## 4.2 *In situ* diffraction measurements

In order to perform the surface sensitive x-ray diffraction measurements, a number of experimental prerequisites are to be fulfilled, i.e., high intensity x-ray radiation and, depending on the purpose of the experiment, special environments for the sample are often needed. In the following section, we will discuss how these conditions were met in this thesis employing synchrotron radiation. The equipment and beamlines where the diffraction measurements have been performed are described.

### The equipment

#### A. The portable UHV diffraction chamber

A portable UHV diffraction chamber which allows for oxidation experiments to be performed at different temperatures up to 800°C and pressures up to 1 bar of oxygen has been used for the *in situ* SXRD measurements. A photo of the chamber is shown in the Fig. 4.3. The chamber is equipped with a beryllium window (a) having a thickness

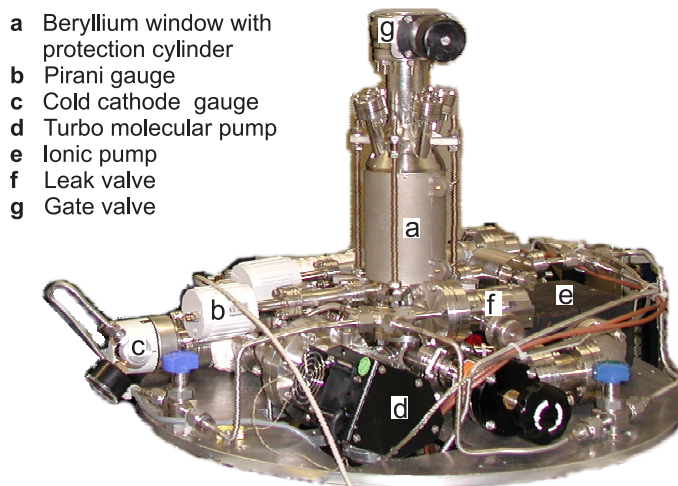


**Figure 4.3:** Portable UHV diffraction chamber.

of 2 mm. The cylindrical shape of the window imposes no limitations for the in-plane diffraction measurements, whereas out-of-plane reflections having exit angles as high as  $54^\circ$  can be reached. In addition, the very low density of Be manifests itself in a reduced attenuation of the x-ray beam, which is an important requirement when performing surface diffraction measurements. During the transportation, the Be window is protected by a metallic cylinder and by four support rods, as can be seen in Fig. 4.3. A gas inlet system is available for supplying different gasses to the sample. During the oxidation experiments, a leak valve (f) was used for precise dosing of the oxygen.

Ultra high vacuum in the  $10^{-9}$  mbar regime can be achieved after baking the chamber at temperatures around  $120^\circ\text{C}$ . The vacuum is maintained by a Varian turbo molecular pump (Turbo-V 70 LP) (d) and a Varion ion getter pump (Star Cell) (e). For the pressure measurement, two different types of gauges were available: the cold cathode ionization gauges and Pirani gauges. The former are capable of measuring pressures between  $10^{-2}$  and  $10^{-10}$  mbar, while the latter works only in the range from atmospheric pressures to  $\sim 10^{-3}$  mbar. On top of the chamber a gate valve (g) is mounted which allows the direct transfer of the sample from the UHV analysis chamber (described in the previous section) into the portable chamber.

## B. High temperature chamber

The high temperature atmospheric oxidation of NiAl(110) was investigated using the commercial Anton Paar HTK 1200 high temperature furnace<sup>2</sup>, shown in Fig. 4.4. The furnace is designed for *in situ* x-ray diffraction studies at ambient pressures and temperatures up

<sup>2</sup>Anton Paar GmbH, A-8054 Graz, Austria; Internet: [www.anton-paar.com](http://www.anton-paar.com).

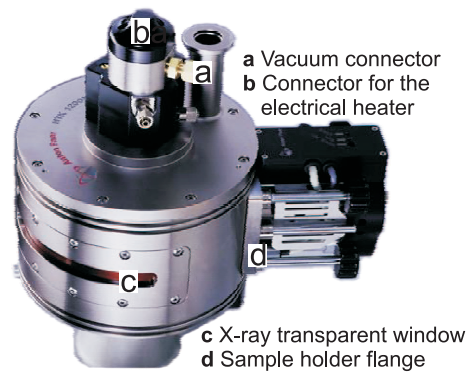


**Figure 4.4:** Anton Paar HTK 1200N high temperature furnace.

to 1200°C. It has a diameter of 150 mm and consists of two foamed  $\text{Al}_2\text{O}_3$  ceramic shells. The sample is heated by a Kanthal APM (22% Cr, 5.8% Al, Fe) heater and the temperature is measured using a Pt 10% RhPt thermocouple inserted axially through the oven body next to the sample holder. The furnace is equipped with a 10 mm wide x-ray transparent window made of Kapton foil. When mounted horizontally, the window allows a rather wide range of in-plane reflections to be accessed (164° degrees in the azimuthal direction). However, its reduced width imposes considerable limitations on the incident and exit angles, therefore this geometry restricts the access to the out-of-plane reflections (those having a non-zero perpendicular momentum transfer). Additional information on the HTK 1200 high temperature furnace can be found at the producer's web site.

## The beamlines

The surface-sensitive x-ray diffraction measurements presented in this thesis have been carried out at two synchrotron sources: the Ångström Quelle Karlsruhe (ANKA) and the European Synchrotron Radiation Facility (ESRF). A brief description of the beamline characteristics is given in the following sections.

### A. MPI-MF Surface Diffraction Beamline at ANKA

The Ångström Quelle Karlsruhe (Fig. 4.2(a)) is a third-generation style electron storage ring located on the site of the Research Center Karlsruhe (FZK), Germany. The storage ring is generally operated at an energy of 2.5 GeV with a typical beam current of 200 mA [60]. The Max Planck Institute for Metals Research (MPI-MF) in Stuttgart runs at ANKA a dedicated beamline for the *in situ* investigation of surfaces, interfaces and thin films, as a general scientific facility. The beamline utilizes synchrotron radiation produced by a bending magnet (BM) with a critical energy of 6 keV. Fig. 4.6 shows a sketch of the beamline layout. The main optical elements are a Rh-coated Si mirror (M) and a

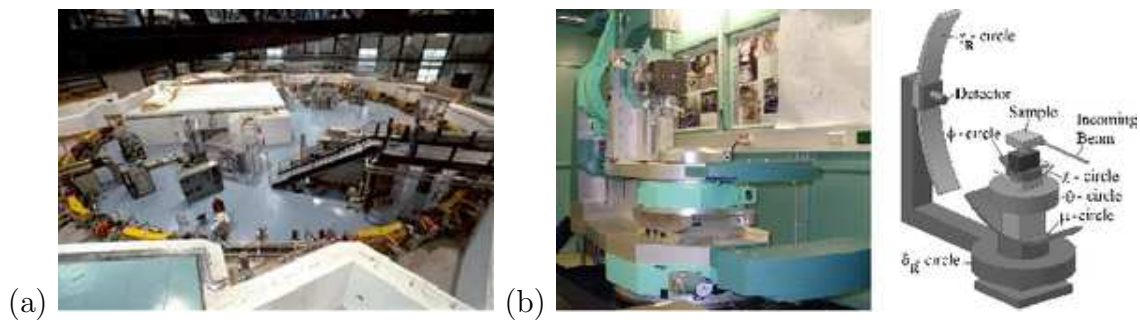


**Figure 4.5:** (a) View of the ANKA hall with the accelerator complex. (b) HUBER diffractometer at the MF-MPI beamline at ANKA [61].

fixed exit height double crystal monochromator (DCM) consisting of a flat Si(111) single crystal and a sagittal Si(111) crystal bender for horizontal focusing. The mirror (M) is needed for harmonic rejection and focusing in the vertical plane. Two pairs of slits (S2, S3) allow to pre-select the beam size on the sample. A conventional scintillation detector has been used for all diffraction measurements presented in this thesis.

**Experimental end-station** The heart of the experimental end station is a specially designed heavy duty HUBER diffractometer that can be operated either in horizontal or vertical sample normal mode. Heavy equipment up to 200 kg (i.e., an UHV or high-temperature chamber) can be placed directly on the goniometer head when mounted vertically. This was the configuration used throughout the measurements presented in this thesis. A photo and a sketch of the diffractometer circles with the goniometer head mounted vertically is shown in the Fig. (b). The diffractometer is controlled by the SPEC software [62]. A detailed description of the beamline and the different diffractometer configurations can be found in [61].

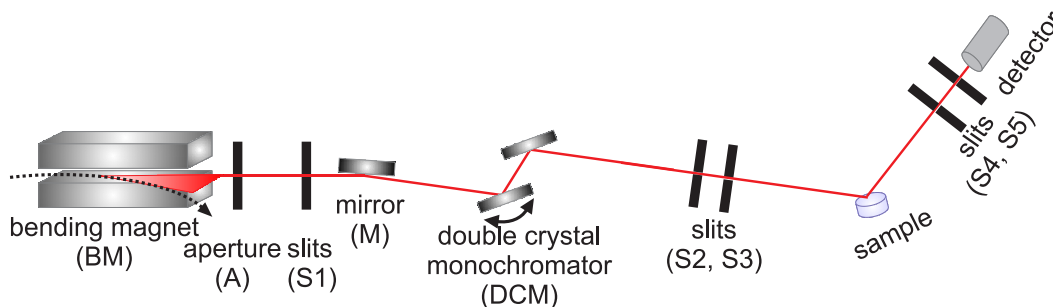


**Figure 4.6:** Schematic layout of the MPI-MF beamline at ANKA [60].

### B. ID32 beamline at ESRF

The ESRF is a third generation synchrotron light source (Fig. 4.7(a)) with a 6 GeV electron storage ring located in Grenoble, France. Our experiments have been performed at the beamline ID32, which is dedicated for surface and interface studies. A schematic layout of the beamline is shown in Fig. 4.8. The beamline utilizes synchrotron radiation produced by an undulator (U). The first optical element is a double crystal monochromator (DCM) [63]. For reducing the heat-load and increasing the beam stability, the first Si(111) crystal is cooled with liquid nitrogen. After the monochromator, a mirror (M) is used for harmonic energy photon rejection.

**Experimental end-station** The experimental end-station for surface diffraction is equipped with a six-circle HUBER diffractometer, shown in Fig. 4.7(b), which allows various sample environments to be used. The diffractometer is controlled by SPEC control software [62]. A Cyberstar scintillation detector has been used for measuring the diffracted intensity. A more detailed description of the beamline characteristics can be found in [64].

### The beamtimes

The x-ray diffraction data presented in this thesis were collected during four experimental runs. More details are listed in the Table 4.1. During the ANKA1 beamtime, the onset of surface oxide grown on the CoGa(100) at different temperatures and partial oxygen pressures was investigated, whereas the transition from the surface gallium oxide to the bulk  $\beta$ -Ga<sub>2</sub>O<sub>3</sub> was studied during the ANKA2 beamtime. The experimental results are presented in Chapter 5. The results on the stability of the ultra-thin aluminium oxide



**Figure 4.7:** [Left] View of the ESRF storage ring. [Right] HUBER diffractometer at the ID32 beamline at ESRF [64].

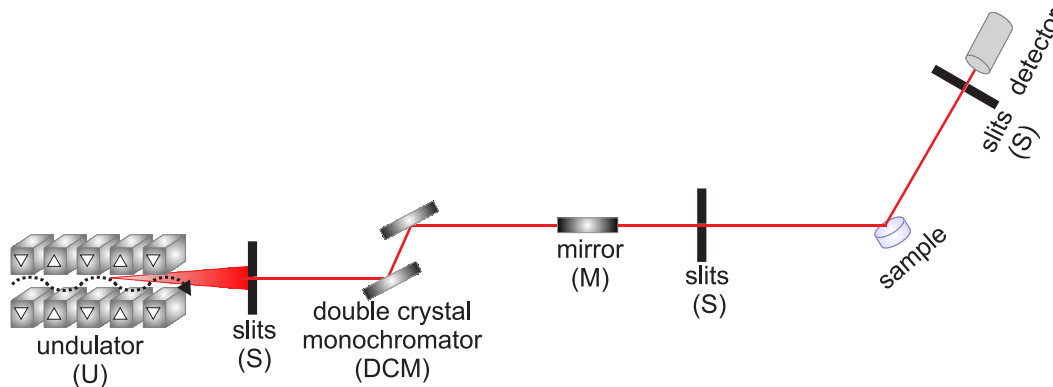


**Figure 4.8:** Schematic layout of the ID32 beamline at ESRF.

layer on NiAl(110) at high oxygen pressures were obtained during the ESRF1 beamtime and are described in the Chapter 6. The atmospheric pressure oxidation of NiAl(110) was investigated during the ANKA3 beamtime and the experimental findings are presented in Chapter 7.

### 4.3 Core-level spectroscopy measurements

Core-level photoemission experiments put great demands on the photon source. A sufficiently high photon energy in combination with a high photon flux are needed to ionize core levels and to keep the measuring times in a reasonable scale. Moreover, the energy resolution has to be high enough to resolve close lying core level components. In order to achieve maximum surface sensitivity the photon energy should be adjustable, so that the kinetic energy of the emitted photoelectrons is in the 50–100 eV range. Therefore, a tunable light source is required to study different elements with different core level binding energies. The core level spectroscopy measurements presented in this thesis were performed at at the I311 beamline at MAX-lab synchrotron radiation facility in Lund, Sweden.

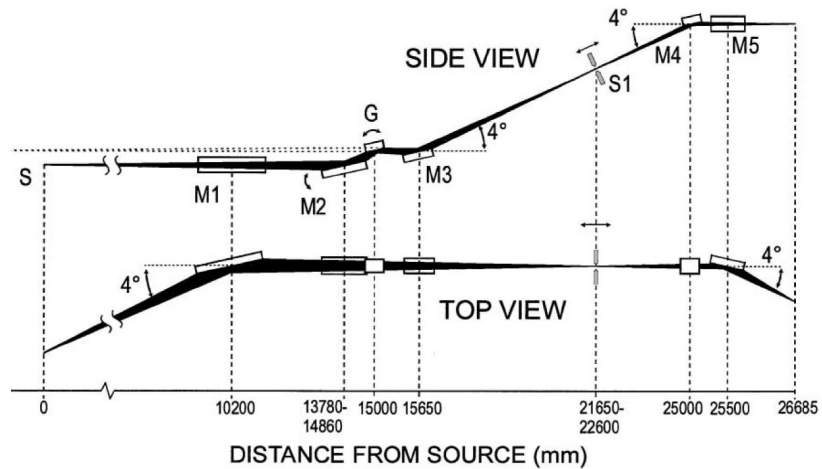
#### I311 beamline at MAX-lab

The beamline I311 is an undulator based soft x-ray (30–1500 eV) beamline dedicated for high resolution core level spectroscopy and x-ray absorption spectroscopy measurements [65]. It utilizes undulator radiation from the 1.5 GeV third generation storage ring, MAX II. The photon flux on the sample is in the range  $10^{11}$ - $10^{13}$  photons per second. The general design of the I311 beamline is illustrated schematically in Fig. 4.9. The first optical element is the pre-mirror (M1), which is used for focusing the beam horizontally prior to the monochromator. A modified SX-700 monochromator is used which consists of

**Table 4.1:** The list of the SXRD experiments performed within this thesis.

Beamtime	Sample	Purpose	Beamline	Energy	Equipment
<b>ANKA1</b>	CoGa(100)	( $p$ - $T$ )-dependent surface oxide formation	MF-MPI	10 keV	portable UHV diffraction chamber
<b>ANKA2</b>	CoGa(100)	transition from surface- to bulk oxide	MF-MPI	10 keV	portable UHV diffraction chamber
<b>ANKA3</b>	NiAl(110)	<i>in situ</i> atmospheric pressure oxidation	MF-MPI	10.5 keV	HTK 1200 HT chamber
<b>ESRF1</b>	NiAl(110)	transition from surface- to bulk oxides	ID32	12.5 keV	portable UHV diffraction chamber

a plane mirror (M2), a plane grating (G) and a spherical focusing mirror (M3). A movable slit (S1) is adjusted whenever the photon energy is changed (this implies the rotation of M2 and G). The beam is then re-focused by a vertically (M4) and a horizontally (M5) deflecting mirror. The energy resolution is changing from about 2 meV at  $h\nu=55$  eV to 150 meV at an incident photon energy of 1000 eV of an exit slit opening of  $10 \mu\text{m}$ . For a more detailed description of the beamline characteristics the reader is referred to [65].

**Figure 4.9:** Schematic layout of the I311 beamline at MAX II [65].

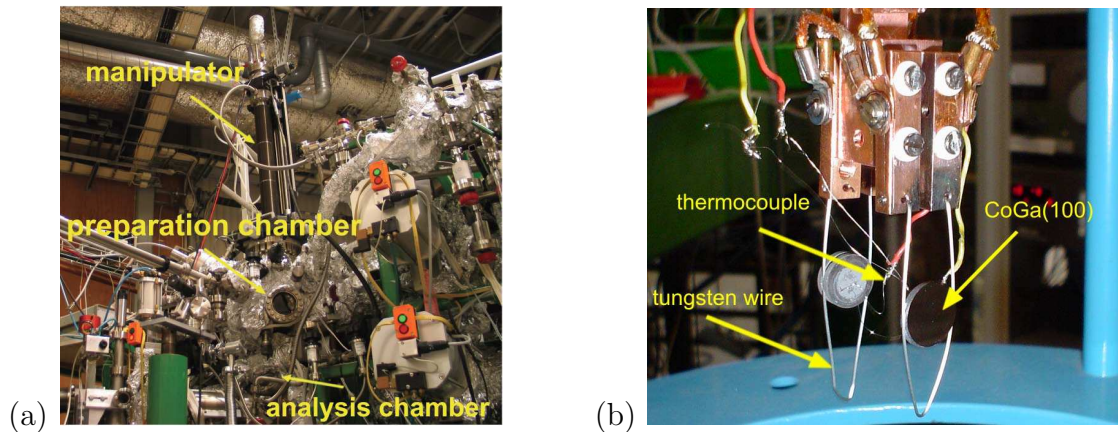


**Figure 4.10:** (a) Experimental set-up for the high resolution core level spectroscopy measurements. (b) The CoGa(100) single crystal mounted on tungsten wires at the end of the long-travel manipulator.

**Experimental end-station** The experimental end-station consists of separate analysis and preparation chambers accessible via a long-travel manipulator, as shown in Fig. 4.10(a). The preparation chamber includes the usual equipment for preparation and characterization of surfaces: gas inlet system, ion sputtering gun and LEED optics. A hemispherical electron energy analyzer SCIENTA SES200 [66] was used for photoelectron spectroscopy measurements. The oxidation of CoGa(100) at different temperatures and oxygen pressures was investigated by HRCLS during one experimental run at the I311 beamline. The CoGa(100) single crystal was mounted on tungsten wires as shown in Fig. 4.10(b). The sample could be heated by passing an electrical current through the support wires or cooled down to liquid nitrogen temperature. The temperature was measured by a Chromel-Alumel thermocouple spot-welded on the back-side of the crystal. The sample preparation procedure was successfully applied for removing the contaminants in the near-surface region. The cleanliness of the sample was monitored by photoemission measurements and the surface structure was checked by LEED.

# Chapter 5

## Structural and physical properties of material systems

### 5.1 The Co-Ga system

The CoGa binary phase diagram is shown in Fig 5.1. There are two intermetallic compounds,  $\beta$ -CoGa and  $\text{CoGa}_3$ , and terminal phases of  $\alpha$ -cobalt (fcc),  $\epsilon$ -cobalt (hcp) and  $\alpha$ -gallium (ortho). The  $\beta$ -CoGa phase has a relatively wide homogeneity range with a maximum at the temperature of the reaction  $\text{Ga (liquid)} + \beta \rightarrow \text{CoGa}_3$ . At  $723^\circ\text{C}$  the homogeneity range of the  $\beta$  phase is from about 27 to 64.5 at.% Ga.

#### $\beta$ -CoGa

The ordered  $\beta$ -CoGa intermetallic compound has a wide homogeneity range, being stable between 44 and 65 at.%Co and the stoichiometric composition melts at  $1210^\circ\text{C}$  [67].  $\beta$ -CoGa crystallizes in a CsCl-type (B2) that forms by two interpenetrating simple cubic lattices. The lattice constant of the stoichiometric composition at room temperature is 0.2878 nm. The  $\beta$ -CoGa(100) unit cell is shown in the inset of Fig. 5.1. When seen along the [001] direction, the structure consists of alternating layers of pure Co and pure Ga.

The defect structure of CoGa is very similar to the one of NiAl [see Section 5.3], two point defects being predominant: vacancies in the cobalt sublattice,  $V^{\text{Co}}$  and substitutional cobalt atoms on the gallium sublattice. The latter are the so-called anti-site defects where the anti-site atom,  $\text{Co}^{\text{Ga}}$ , is surrounded by eight Co atoms. Therefore, in the Co-rich side the anti-site Co atoms are present, while in the Ga-rich side the deviation from stoichiometry is accompanied by formation of Co vacancies,  $V^{\text{Co}}$ . Consequently a triple defect consisting of two vacancies on the transition metal sublattice combined with one anti-site atom on the gallium sublattice has been generally accepted [68]. In addition, it was reported that the electrical and magnetic properties of  $\text{Co}_x\text{Ga}_{1-x}$  compounds can

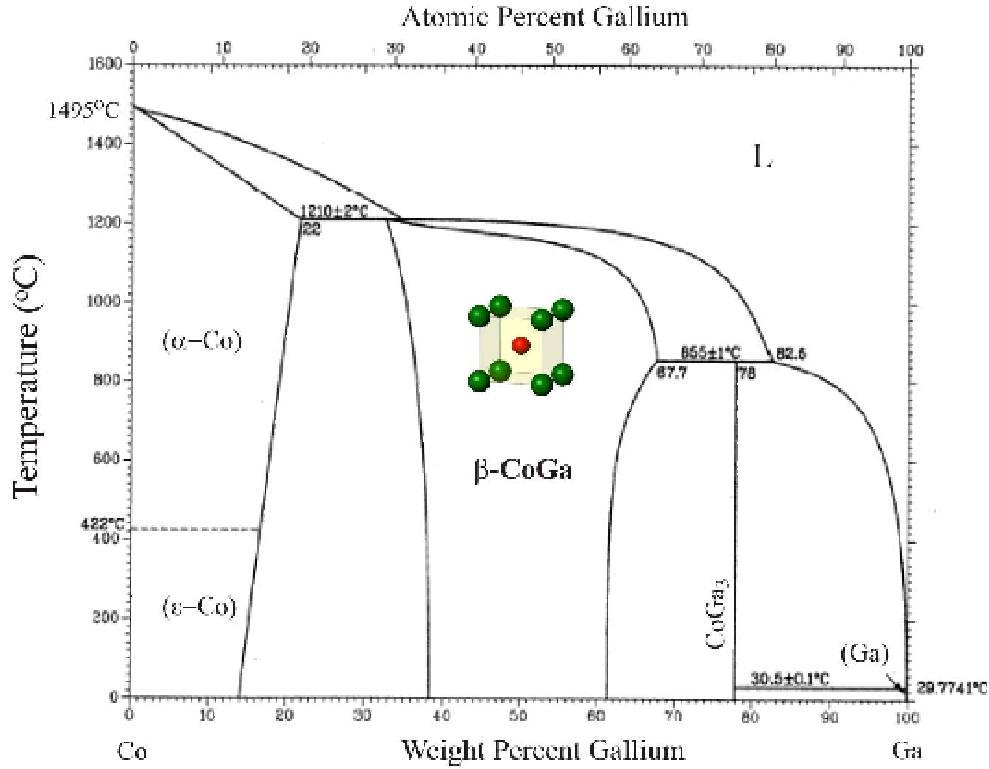


**Figure 5.1:** The phase diagram of the Co-Ga system [67].

be attributed to their defect content, which depends on the annealing-cooling treatment. Each Co anti-site defect is associated with a magnetic moment of approximately  $5 \mu_B$ .

## 5.2 Bulk $\text{Ga}_2\text{O}_3$ phases

$\text{Ga}_2\text{O}_3$  exists in different phases based on the closed packed oxygen lattices [69, 70]. Most of the  $\text{Ga}_2\text{O}_3$  phases are isomorphic to the appropriate  $\text{Al}_2\text{O}_3$  phases (see Section 5.4). The structural characteristics of some of these phases are listed in the Table 5.1.

$\alpha\text{-Ga}_2\text{O}_3$  forms in the corundum structure where the oxygen ions form a hcp sublattice and the gallium ions are accommodated exclusively in the octahedral sites. Another group of gallium oxides are those characterized by a fcc oxygen sublattice. The  $\text{Ga}^{3+}$  ions occupy both octahedrally and tetrahedrally coordinated sites. The modifications of  $\gamma\text{-Ga}_2\text{O}_3$ ,  $\delta\text{-Ga}_2\text{O}_3$  and  $\beta\text{-Ga}_2\text{O}_3$  belong to this group.

The only thermodynamically stable gallium oxide phase is known to be  $\beta\text{-Ga}_2\text{O}_3$ . This is also the only gallia phase encountered in the present work, therefore some of its properties will be given in the next section.

**Table 5.1:** Crystal structures of some gallia phases [69].

Oxide	Space Group	Unit cell parameters	Oxygen sublattice	Occupied interstices	Remarks
$\alpha$ -Ga <sub>2</sub> O <sub>3</sub>	hexagonal D <sub>3d</sub> <sup>6</sup>	a=4.983 Å c=13.43 Å	hcp	octahedral	Corundum
$\beta$ -Ga <sub>2</sub> O <sub>3</sub>	monoclinic C2/m	a=12.21 Å b=3.04 Å c=5.80 Å $\beta$ =103.83°	fcc	octahedral+ tetrahedral	isomorph with $\theta$ -Al <sub>2</sub> O <sub>3</sub>
$\gamma$ -Ga <sub>2</sub> O <sub>3</sub>	cubic O <sub>h</sub> <sup>7</sup>	a=8.22 Å	fcc	octahedral+ tetrahedral	Spinel-Type
$\delta$ -Ga <sub>2</sub> O <sub>3</sub>	cubic	a=9.52 Å	fcc	octahedral+ tetrahedral	distorted Spinel-Type

### $\beta$ -Ga<sub>2</sub>O<sub>3</sub>

The monoclinic crystal structure of  $\beta$ -gallium oxide is depicted in Fig. 5.2. It contains two crystallographically different Ga atoms in the asymmetric unit, one with tetrahedral (magenta spheres) and the other with octahedral (red spheres) coordination geometry. The oxygen ions (blue spheres) form a distorted cubic close packed lattice. The O–Ga–O angles in the tetrahedral arrangements are in the range 105.92–119.59°. The Ga–O distances are in the range 1.833–1.863 Å and 1.935(2)–2.074(1) Å within the tetrahedral and octahedral arrangements, respectively [71].  $\beta$ -Ga<sub>2</sub>O<sub>3</sub> has a density of 5.961 g/m<sup>3</sup> [72, 69, 73]. The melting point was reported to be 1740°C.  $\beta$ -Ga<sub>2</sub>O<sub>3</sub> single crystals can be grown by the floating zone method [74].  $\beta$ -Ga<sub>2</sub>O<sub>3</sub> is intrinsically an insulator with a band gap of 4.8 eV [75] and it is an n-type semiconductor when synthesized under reducing conditions (due to a slight oxygen deficit within the crystal lattice).

## 5.3 The Ni-Al system

The phase diagram assessed for the Al-Ni system is shown in Fig. 5.3. It consists of two fcc solid solutions, Al and Ni, and five intermetallic phases: AlNi<sub>3</sub>, AlNi, Al<sub>3</sub>Ni<sub>2</sub>, Al<sub>3</sub>Ni, and Al<sub>3</sub>Ni<sub>5</sub>. The solid solubility of Ni in Al is very limited, but was reported to decrease from 0.11 at.% Ni at the 640°C to 0.01 at.% Ni at 500°C. Ni dissolves Al in solid solution up to a maximum of 21.2 at.% at 1385°C.

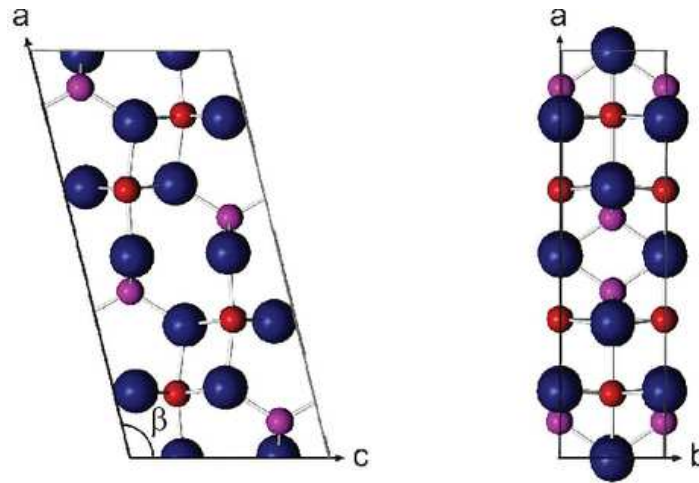


**Figure 5.2:** The real space unit cell of  $\beta$ -Ga<sub>2</sub>O<sub>3</sub>. The Ga atoms occupying the tetrahedral and octahedral sites are represented by the magenta and red spheres, respectively. The oxygen ions are shown as blue spheres.

### $\beta$ -NiAl

The intermetallic  $\beta$ -NiAl phase exhibits a wide single phase field and the stoichiometric composition melts at 1638°C. NiAl possesses the ordered cubic B2 (CsCl prototype) crystal structure, which consists of two interpenetrating primitive cubic cells, where Al atoms occupy the cube corners of one sublattice and Ni atoms occupy the cube corners of the second sublattice (see inset in Fig. 5.3).

The lattice constant of the stoichiometric composition at room temperature is 0.2887 nm [76]. A maximum in the lattice constant is noted either at the stoichiometric composition [76] or for slightly non-stoichiometric alloys [77] and lower values for the lattice constants are observed on either side of stoichiometry. The density of stoichiometric NiAl at room temperature is 5.85 g/cm<sup>3</sup>. An increase in the density is observed to take place with increasing Ni content (6.6 g/cm<sup>3</sup> at 61.9 at.% Ni), but it rapidly decreases as Ni is removed from the stoichiometric alloy [76].

The B2 structure is stable for large deviations from stoichiometry, and significant long-range order is reported for both Ni-rich and Al-rich compositions [78]. On the Ni-rich side it was found that aluminum atoms are replaced substitutionally by nickel atoms (Ni anti-site atoms). This explains the aforementioned decrease in the lattice parameter which was found to be proportional to the Ni excess. Also, since nickel is much heavier than aluminum, the density of the alloys increases with rising nickel concentration. On the Al-rich side of NiAl instead of aluminum replacing nickel atom by atom and thereby producing an increase in the lattice parameter, there is a decrease in the lattice constants coupled with a rapid fall in the density. The reason is that the deviation from the stoichiometry

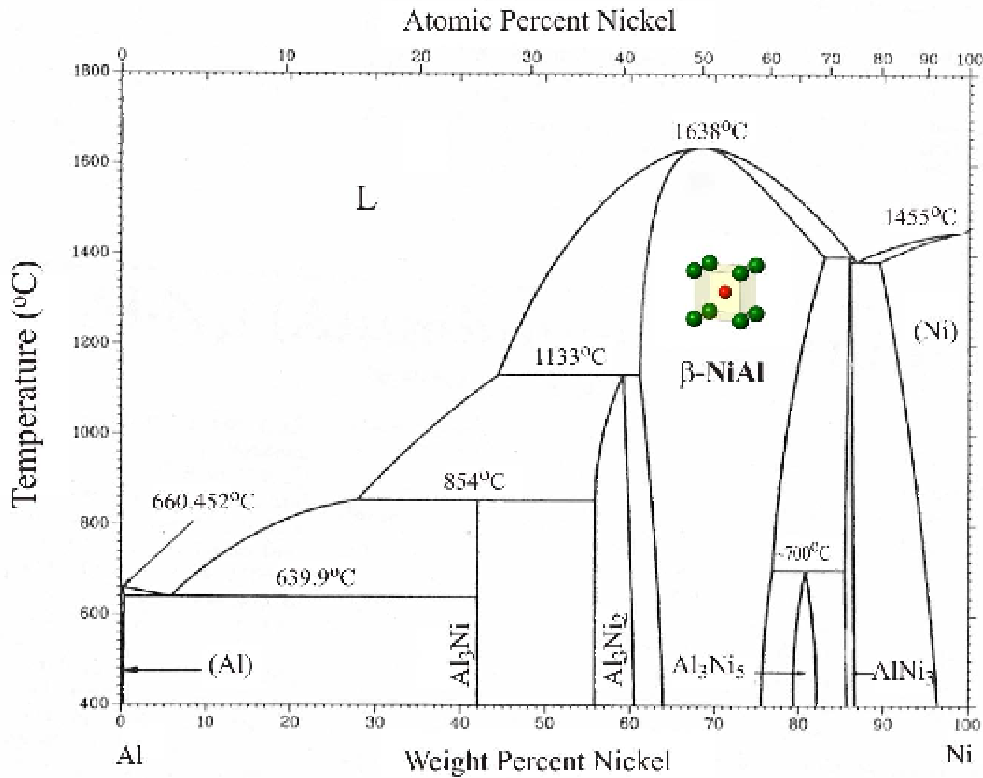


**Figure 5.3:** The phase diagram of the Ni-Al system [67].

is in this case accommodated by the existence of vacancies on the Ni sublattice [79, 68, 80, 81].

According to theoretical studies, Al anti-site defects and vacancies on the Al sublattice are energetically unfavorable, and their concentrations are therefore supposed to be very low throughout the entire NiAl phase field. For a comparison, the energies of vacancies and anti-site defects reproduced from Ref. [82] are listed in the Table 5.2. In contrast to these results, several experimental studies reported the existence of both Al anti-site atoms and Al vacancies [80, 81].

Due to its properties, NiAl is the basis of a family of alloys long-used as coating materials for oxidation and corrosion resistance at high temperatures in gas turbine engines. The advantages associated with NiAl as a candidate structural material in advanced gas turbine engines include a 30% reduction in density over the Ni-based superalloys and a good intrinsic environmental resistance. NiAl alloys have larger thermal conductivities and melting temperatures than the Ni-base superalloys which means improved cooling efficiency and higher operating temperatures. The good oxidation resistance is manifested in the formation of a protective alumina layer. The different polymorphs of alumina are discussed in the following section. For more detailed information concerning the physical and mechanical properties of NiAl system the reader is referred to Ref. [78].

**Table 5.2:** Energies of vacancies and anti-site defects in NiAl.

Defect type	Energy (eV)
Ni vacancy	1.36
Al vacancy	1.03
Ni antisite	1.94
Al antisite	-0.89

## 5.4 Bulk $\text{Al}_2\text{O}_3$ phases

Aluminium oxides are ceramic materials of extremely high technological importance and can be produced by thermal treatment of aluminum hydroxides [83, 84], which are commonly found in nature. On the other hand, oxidation of aluminum and aluminium-containing alloys results in the formation of aluminum oxide, which may actually protect the metal from further oxidation.

$\text{Al}_2\text{O}_3$  shows polymorphism and at least 15 varieties of transient phases are known [69] besides the thermodynamically stable  $\alpha\text{-Al}_2\text{O}_3$  (corundum). All alumina phases consist of a close-packed oxygen sublattice which can be either face-centered cubic (fcc) as in the case of  $\gamma\text{-}$ ,  $\eta\text{-}$ ,  $\delta\text{-}$ ,  $\theta\text{-Al}_2\text{O}_3$  or hexagonal-close packed (hcp) in  $\alpha\text{-}$ ,  $\kappa\text{-}$ ,  $\chi\text{-Al}_2\text{O}_3$ . On this basic lattice the  $\text{Al}^{3+}$  ions are placed on different positions with octahedral and tetrahedral coordination. Within each subgroup, it is only the ordering of the  $\text{Al}^{3+}$  ions that gives rise to different polymorphs. Despite the fact that extensive work has been carried out over past decades to characterize the structure of these polymorphs [85], structural information on some metastable alumina phases is still lacking or controversial, and phase transformation mechanisms are poorly understood.

### $\alpha\text{-Al}_2\text{O}_3$

The crystal structure of  $\alpha\text{-Al}_2\text{O}_3$  was determined in 1925 by Linus Pauling and Sterling Hendricks [86]. It forms in a corundum structure and there are two types of unit cells which can be considered: hexagonal and rhombohedral [87, 85]. The rhombohedral unit cell is composed of two  $\text{Al}_2\text{O}_3$  molecular units. The structure is more easily visualized, considering a hexagonal unit cell composed of six molecular units (30 atoms). The hexagonal structural unit cell is characterized by  $a=b=4.7589 \text{ \AA}$ ,  $c=12.991 \text{ \AA}$ ,  $\alpha=\beta=90^\circ$  and  $\gamma=120^\circ$  and it is shown in Fig. 5.4 (viewed perpendicular to the  $[11\bar{2}0] \parallel [0001]$  plane). The oxygen and aluminium ions are represented by the blue and red spheres, respectively. In the  $[0001]$  direction  $\alpha\text{-Al}_2\text{O}_3$  is composed of approximately hexagonal close packed

**Table 5.3:** Crystal structures of some alumina phases [69].

Oxide	Spatial Group	Unit cell parameters	Oxygen sublattice	Occupied interstices	Remarks
$\alpha$ -Al <sub>2</sub> O <sub>3</sub>	hexagonal D <sub>3d</sub> <sup>6</sup>	a=4.76 Å c=12.99 Å	hcp	octahedral	Corundum
$\kappa$ -Al <sub>2</sub> O <sub>3</sub>	hexagonal	a=9.71 Å c=17.86 Å		octahedral+ tetrahedral	
$\gamma$ -Al <sub>2</sub> O <sub>3</sub>	cubic O <sub>h</sub> <sup>7</sup>	a=7.911 Å	fcc	octahedral+ tetrahedral	Spinel-Type
$\delta$ -Al <sub>2</sub> O <sub>3</sub>	tetragonal	a=7.96 Å c=11.70 Å	fcc	octahedral+ tetrahedral	distorted Spinel-Type
$\theta$ -Al <sub>2</sub> O <sub>3</sub>	monoclinic C <sub>2h</sub> <sup>3</sup>	a=2.92 Å b=5.64 Å c=11.83 Å $\beta=103^\circ$	fcc	octahedral+ tetrahedral	isomorph with $\beta$ -Ga <sub>2</sub> O <sub>3</sub>
$\beta$ -Al <sub>2</sub> O <sub>3</sub>	hexagonal	a=5.60 Å c=22.50 Å		octahedral+ tetrahedral	

O<sup>2-</sup> layers forming a *ABAB* hcp stacking sequence, as shown in Fig.5.4. The oxygen ion planes are alternating with buckled aluminium ion planes. The aluminium ions occupy  $\frac{2}{3}$  of the octahedral sites present between the oxygen layers. In each layer the cations arrange themselves in one of three types of the hexagonal network, which differ in the position of the vacant octahedral site. The hexagonal networks in successive Al layers are shifted laterally by one octahedral site, such that their stacking sequence along [0001] is *ABCABC...* The Al cations are displaced along the [0001] direction toward the neighboring empty octahedral site, resulting in a rumpling of the cation layers. The Al ion displacements are accompanied by the distortion of the oxygen sublattice.

### Metastable aluminas

Due to their special properties and high transition temperatures (above 500°C), the metastable aluminas have received a lot of technological attention. They are characterized by high surface area and fine particle size, which opens up the possibility to be used as adsorbents, catalyst supports, coatings, and soft abrasives. Also, there is increased interest in the transformation mechanism between the different alumina phases due to the application of  $\alpha$ -Al<sub>2</sub>O<sub>3</sub> as a protective oxide scale on the surface of high-temperature al-

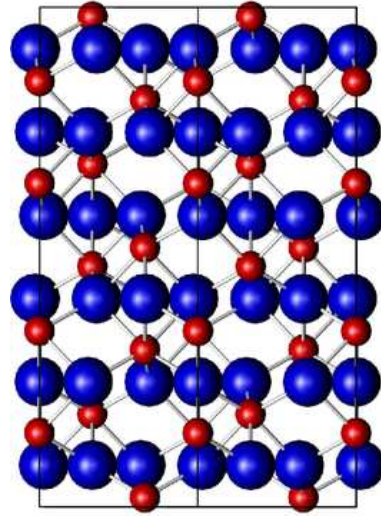


**Figure 5.4:** The unit cell of  $\alpha\text{-Al}_2\text{O}_3$  viewed perpendicular to the  $[11\bar{2}0] \parallel [0001]$  plane. The oxygen and aluminium ions are represented by the blue and red spheres, respectively.

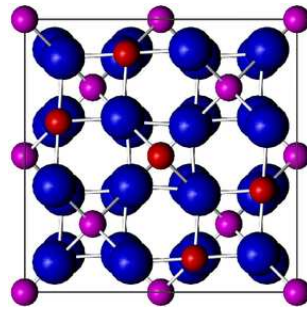


**Figure 5.5:** The unit cell of  $\gamma\text{-Al}_2\text{O}_3$  (view perpendicular to the  $[100] \parallel [001]$  plane). The Al atoms occupying the tetrahedral and octahedral sites are represented by the magenta and red spheres, respectively. The oxygen ions are shown as blue spheres.

loys. A stable scale formation is promoted by the high temperature oxidation of the alloy and an understanding of the fundamental aspects of the transition between the metastable to  $\alpha$ -alumina is therefore essential.  $\gamma\text{-Al}_2\text{O}_3$  and  $\delta\text{-Al}_2\text{O}_3$  are the two metastable alumina phases we have encountered in our study, therefore a short structural description will be given below.

### $\gamma\text{-Al}_2\text{O}_3$

$\gamma\text{-Al}_2\text{O}_3$  has been commonly presented as a defect spinel type structure with  $Fd\bar{3}m$  space group and has a lattice constant of  $\mathbf{a}_0=7.8217 \text{ \AA}$ . The oxygen anions form a fcc sublattice and  $\text{Al}^{3+}$  ions occupy octahedrally and tetrahedrally coordinated sites [85]. The unit cell of  $\gamma\text{-Al}_2\text{O}_3$  is shown in Fig. 5.5. The oxygen ions are represented by the blue spheres and the octahedrally and tetrahedrally coordinated aluminium ions are represented by the red and magenta spheres, respectively.

Due to the stoichiometry, not all cation sites can be occupied by Al<sup>3+</sup> ions in an Al<sub>2</sub>O<sub>3</sub> compound having the spinel structure: there are 32 O<sup>2-</sup> ions forming a fcc sublattice, leaving, then,  $\frac{2}{3} \times 32 = 21 \times \frac{1}{3} \text{Al}^{3+}$  ions to fill the cation sites. In the spinel structure, the interstitial sites occupied by Al<sup>3+</sup> ions are restricted to the *8a* (tetrahedral) and *16d* (octahedral) Wyckoff positions. However, there is uncertainty regarding the occupancy of the cation sites, including the relative distribution of the Al ions between the tetrahedral and octahedral sites [88, 89, 90]. Many studies show a preference of Al ions for tetrahedral sites. Others provide evidence for the opposite, with a preference for occupation of octahedral sites. In addition, some authors suggest that there is a significant portion of Al atoms occupying non-spinel sites. Recent models based on neutron scattering [91, 92] and *ab initio* calculations [91] propose also a tetragonal model for the structure of boehmite-derived  $\gamma$ -Al<sub>2</sub>O<sub>3</sub> with *I*<sub>4</sub>1/*amd* space group symmetry with Al cations placed on non-spinel sites.

### $\delta$ -Al<sub>2</sub>O<sub>3</sub>

$\delta$ -Al<sub>2</sub>O<sub>3</sub> has been described as a superlattice of the spinel structure with ordered cation vacancies composed of a tripled spinel unit cell with 160 atoms per unit cell [85]. Two possible unit cells have been suggested: either tetragonal with the lattice parameters  $a=b=a_\gamma$  and  $c=3a_\gamma$  [84] or orthorhombic with  $a=a_\gamma$ ,  $b=1.5a_\gamma$  and  $c=2a_\gamma$  [88]. In all reports the tetragonal  $\delta$  unit cell has been derived from boehmite, whereas the orthorhombic  $\delta$  unit cell has been observed for precursors obtained either by quenching of the melt or by thermal oxidation. The existence of the tetragonal structure of  $\delta$ -Al<sub>2</sub>O<sub>3</sub> is still controversial: some reports point toward the true unit cell being orthorhombic and explain the occurrence of results which indicate the tetragonal unit cell as being caused by a misinterpretation of the experimental data. However, the *d*-spacings of the observed  $\delta$ -alumina reflections in our diffraction experiments correspond to those of the tetragonal structure reported in Ref. [84].



# Chapter 6

## Oxidation of CoGa(100)

The formation of a crystalline thin gallium oxide film was previously observed by exposing the CoGa(100) surface at relatively low oxygen partial pressures and temperatures higher than 280°C [26, 27]. Such ultra-thin oxide films are discussed as potential candidates for insulating barriers between two ferromagnetic layers in magnetic RAMs. Besides having the desired properties, one of the requirements for practical applications is that the oxide layer should be homogeneous, stable and reproducible in thickness and composition.

This chapter deals with the structure and the stability of the oxide layers grown on CoGa(100) surface under different oxidation conditions. The core of this study comprises experimental observations based on surface x-ray diffraction and high resolution core level spectroscopy measurements. In addition, low energy electron diffraction and atomic force microscopy experiments served for characterization of the surface structure and morphology. These experimental tools have been complemented with density functional theory-based calculations which yield information on the oxide phases stability and the core level shifts<sup>1</sup>.

The chapter is organized as follows: In the section 6.1, a brief account of the previous CoGa(100) oxidation studies is given. The experimental details of the surface x-ray diffraction and high resolution core level spectroscopy measurements are described in the section 6.2. Using a multi-technique approach, an atomic level understanding of the structure of the surface gallium oxide layer has been achieved. The new structural model is discussed in the section 6.3.1. A comparison with other plausible structural models tested by SXRD, HRCLS and DFT-based calculations is shown. The section 6.3.3 comprises the results on the onset of surface oxide formation at different temperatures. *In situ* SXRD measurements allowed us to follow the transition from the surface oxide to the bulk  $\beta$ -Ga<sub>2</sub>O<sub>3</sub> oxide at different temperatures and pressures ranging from the 10<sup>-7</sup> mbar up to

---

<sup>1</sup>The density functional theory calculations have been performed by Georg Kresse and Martijn Marsman, Institut für Materialphysik, Universität Wien.

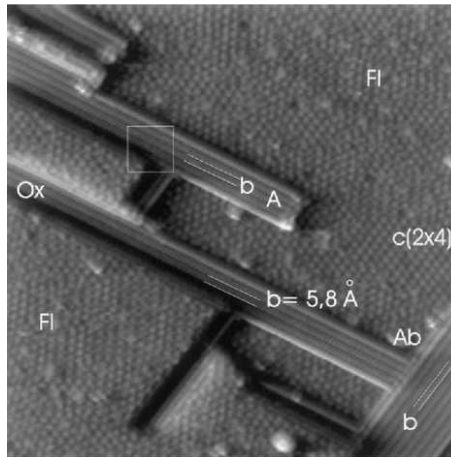


**Figure 6.1:** STM image after oxidation with 1 L  $O_2$  of CoGa (100) at 430°C ( $320 \times 320 \text{ \AA}^2$ ) [26].

ambient pressures. The results are summarized in section 6.3.4. Section 6.3.5 deals with the high temperature oxidation regime, when the growth of the bulk oxide has been observed to be accompanied by substrate faceting. The chapter concludes with a summary.

## 6.1 Introduction

The initial stages of thin gallium oxide growth on CoGa(100) have been previously studied by means of STM, HREELS, AES and LEED measurements [26, 93, 94]. It has been observed that room temperature oxygen exposure leads to the formation of amorphous oxide films, which may be crystallized upon subsequent annealing. At temperatures higher than 280°C and low oxygen partial pressures the oxide islands start to form mainly at the step edges of the terraces [95]. The islands were observed to have a long rectangular shape and to be preferentially oriented in the [100] and [010] directions of the substrate. Fig. 6.1 shows an STM image obtained after 1 L<sup>2</sup> oxygen exposure ( $\sim 1000$  seconds at  $10^{-9}$  mbar  $O_2$ ) at 430°C [26]. *Fl* marks the substrate areas which are not oxidized, whereas *Ox* represents oxide islands which start to grow at a step edge.

Based on a previous SXRD study [96], an atomistic model of the surface gallium oxide layer was proposed. However, the structure of the oxide/substrate interface appeared as not being accurately reproduced by this model. In addition, recent DFT-based calculations rendered this model as energetically unfavorable. Additional core level spectroscopy measurements have been performed. In the present work, a new structural model has been proposed based on a multi-technique approach. These results will be discussed in the section 6.3.1. Recent *in situ* x-ray diffraction investigations [97] revealed an  $O_2$  pres-

<sup>21</sup> 1 Langmuir (L)  $\sim 10^{-6}$  mbar·s.

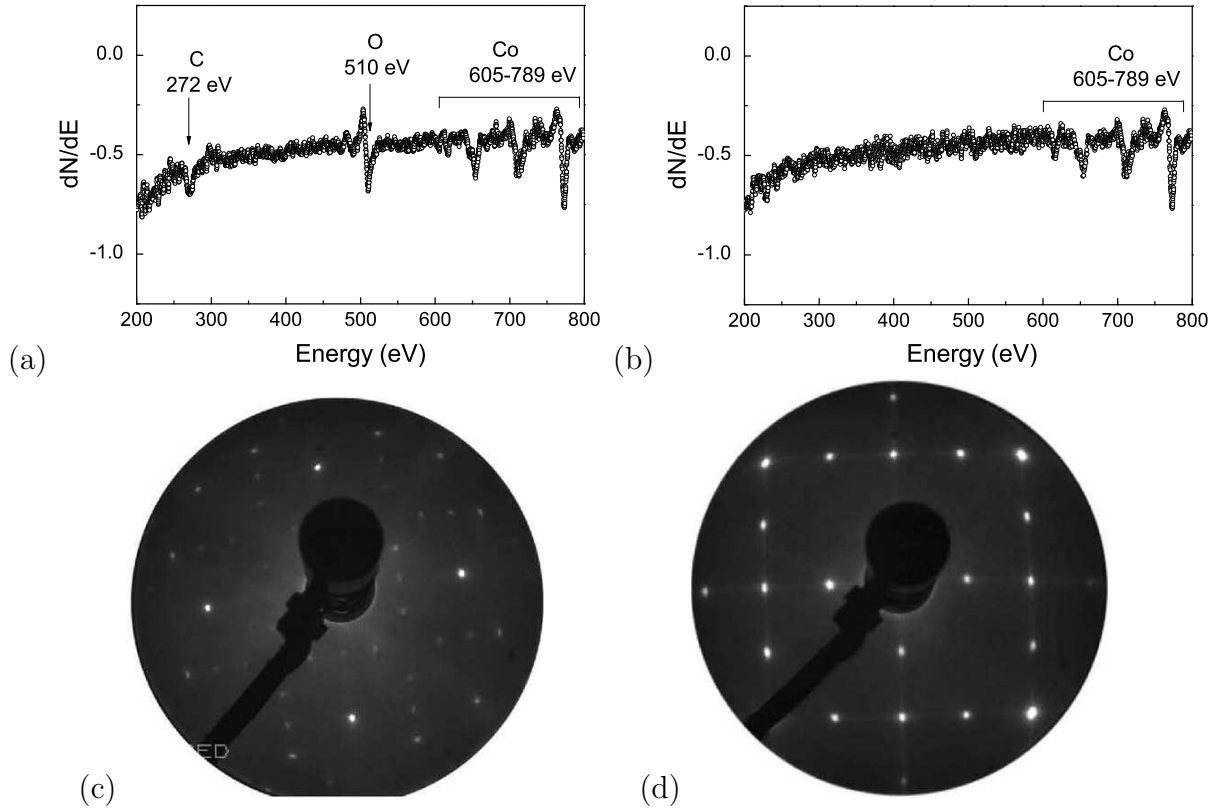


**Figure 6.2:** Auger electron spectra recorded for the CoGa(100) (a) before and (b) after the cleaning procedure. (c) LEED pattern of the  $c(4 \times 2)$  reconstruction of clean CoGa(100) surface recorded at an electron energy of 88 eV. (d) LEED pattern of the surface oxide layer on CoGa(100) recorded at an electron energy of 83 eV.

sure dependent transition from a layer-by-layer growth mode to a step flow growth mode. However, the stability of the surface oxide as a function of temperature and partial oxygen pressure had been still an open issue and was dealt with within the present work.

## 6.2 Experimental details

### Sample preparation

A nominally  $\text{Co}_{50}\text{Ga}_{50}$  single crystal with a diameter of 10 mm and a thickness of 2 mm has been used for all the experiments described in this chapter. The specimen has been cut parallel to the (100) planes and oriented by x-ray diffraction better than  $0.1^\circ$ . It has been polished on one side using alumina paste down to  $0.05 \mu\text{m}$ . Fig. 6.2(a) shows the AES spectrum recorded from the CoGa(100) sample before cleaning. The AES signal at 272 and 510 eV indicates a contamination with carbon and oxygen, respectively. Heating the sample in an oxygen atmosphere at  $500^\circ\text{C}$  leads to the oxidation of the sample surface and of the carbon impurities. The surface oxides formed in this way were desorbed by

**Table 6.1:** Typical parameters for the oxidation, desorption, Ar<sup>+</sup>-sputtering and annealing procedures during the CoGa(100) surface preparation.

Oxidation	Temperature	500°C
	Partial oxygen pressure	$6.6 \times 10^{-6}$ mbar
	Time	600 s
Oxide desorption	Temperature	600°C
	Time	600 s
Ar <sup>+</sup> -sputtering	Ion energy	1000 eV
	Ion current	10–15 $\mu$ A
	Time	1800 s
Annealing	Temperature	800°C
	Time	600 s

annealing at 800°C. Several cycles of oxidation-desorption and sputtering-annealing were necessary in order to create an impurities-depleted surface region. No signal from carbon or oxygen was detected after the cleaning procedure was completed [Fig. 6.2(b)]. The parameters characteristic for an optimal preparation procedure are given in the Table 6.1.

The LEED pattern of the clean CoGa(100) surface exhibits a  $c(4 \times 2)$  reconstruction in two domains rotated by 90°, as can be seen in Fig. 6.2(c). The oxidation at 500°C and  $6.6 \times 10^{-6}$  mbar leads to the formation of a surface gallium oxide layer. The LEED pattern in Fig. 6.2(d) shows a  $(2 \times 1)$  superstructure in two domains rotated by 90°, corresponding to oxide islands being preferentially oriented along two substrate directions perpendicular on each other.

## Surface x-ray diffraction measurements

The SXRD measurements were performed at the MPI-MF dedicated beamline at ANKA, Germany<sup>3</sup>. A photon energy of 10 keV was used for both experiments. The sample was mounted inside the portable UHV diffraction chamber, allowing oxidation experiments to be performed at partial oxygen pressures up to 1 bar. The diffraction chamber was also equipped with an Ar<sup>+</sup>-sputtering gun, which facilitated the preparation of a clean substrate surface. The sample was heated using an alumina encapsulated radiative heater. During the ANKA1 beamtime the sample temperature was estimated using a Chromel-

<sup>3</sup>The SXRD data presented in this chapter were collected during the beamtimes ANKA1 and ANKA2, as described in Chapter 4.

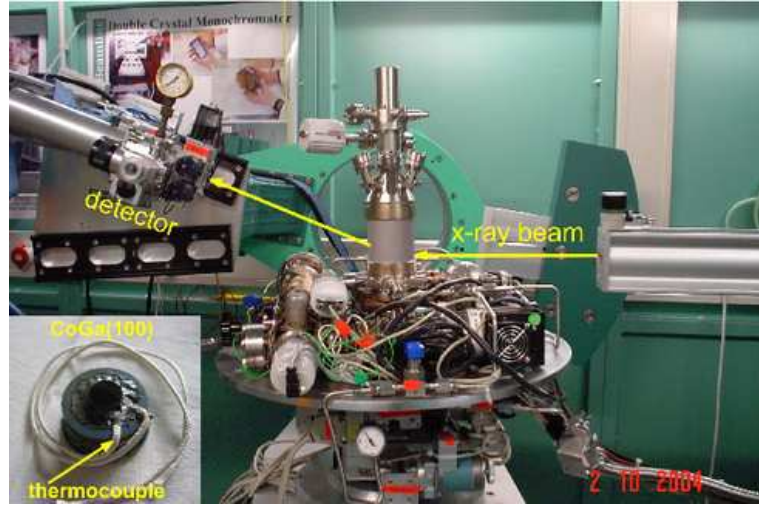


**Figure 6.3:** Typical set-up for the SXRD measurements at ANKA.

Alumel thermocouple mounted behind the portable sample holder. The oxide desorption temperature was used as a reference for temperature calibration. A more accurate control of the sample temperature was achieved during the ANKA2 beamtime by spot-welding the thermocouple directly on the CoGa crystal. An image of the sample mounted on the inconel sample holder having the thermocouple attached on the side of the crystal is shown in the inset of Fig. 6.3.

### Reciprocal lattice of CoGa

During the x-ray diffraction measurements the orientation matrix was set with respect to the reciprocal lattice of the substrate. The lattice parameters describing the CoGa unit cell are  $a=b=c=2.878 \text{ \AA}$  and  $\alpha=\beta=\gamma=90^\circ$ . The real space unit cell is shown in Fig. 6.4(a). It can be described by a unit cell containing one Co and one Ga atom at  $(0, 0, 0)$  and  $(\frac{1}{2}, \frac{1}{2}, \frac{1}{2})$  lattice sites, respectively. The structure factor takes the form:

$$F_{HKL} = f_{\text{Co}} + f_{\text{Ga}} \exp[\pi i(H + K + L)],$$

where  $f_{\text{Co}}$  and  $f_{\text{Ga}}$  represent the atomic form factors of Co and Ga, respectively. It follows that:

$$\begin{aligned} F_{HKL}^{\text{F}} &= f_{\text{Co}} + f_{\text{Ga}}, & \text{if } H + K + L = \text{even (fundamental reflections),} \\ F_{HKL}^{\text{S}} &= f_{\text{Co}} - f_{\text{Ga}}, & \text{if } H + K + L = \text{odd (superstructure reflections).} \end{aligned}$$

While the reflections with  $H + K + L = \text{odd}$  are forbidden in a simple bcc lattice, in the case of an CsCl-type of structure they arise from the chemical ordering and are being called *superstructure reflections*. The reciprocal lattice of CoGa(100) is shown in Fig. 6.4(b). The

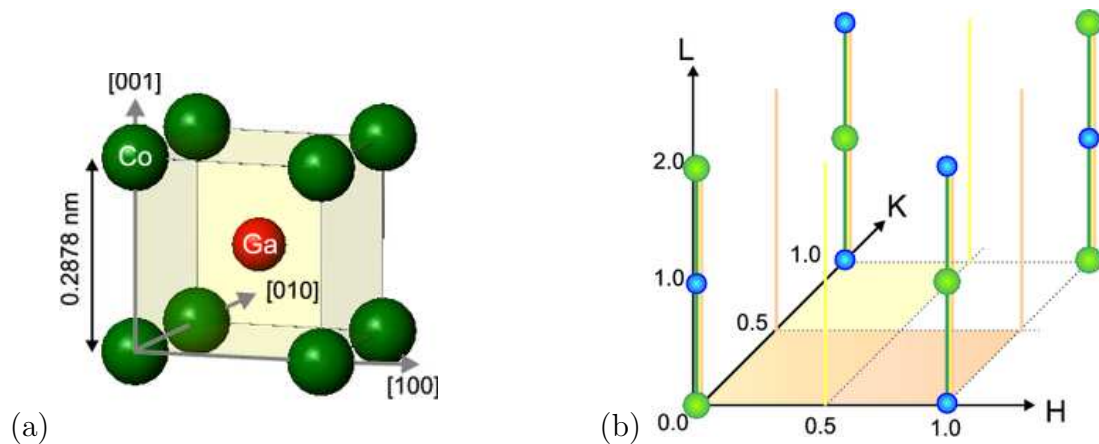


**Figure 6.4:** (a) Real space unit cell of  $\beta$ -CoGa. (b) Reciprocal lattice of the CoGa (green and blue spheres mark the fundamental and superstructure reflections, respectively). Superimposed are the surface rods from the  $(2\times 1)$  and  $(1\times 2)$  surface oxide domains represented by the yellow and orange lines, respectively.

fundamental and the superstructure reflections are marked by the green and blue circles, respectively. The reciprocal lattice vectors are thus  $a^*=b^*=c^*=2.183 \text{ \AA}^{-1}$ . The  $H$  and  $K$  indexes describe the in-plane momentum transfer and the  $L$  index the perpendicular one, expressed in reciprocal lattice units (r.l.u.).

The surface gallium oxide grows epitaxially on the CoGa(100) substrate and forms a  $(2\times 1)$  superstructure in two domains  $90^\circ$  rotated with respect to each other. The oxide layer will exhibit its own reciprocal lattice giving rise to additional rods of scattered intensity at non-integer  $H$  and  $K$  values. The surface rods arising from the  $(2\times 1)$  and  $(1\times 2)$  oxide domains and are indicated in the Fig. 6.4(b) by the yellow and orange lines, respectively. At integer  $H$  and  $K$  values both oxide domains contribute and there is a coherent superposition of the intensity scattered from the oxide and from the substrate. Consequently, the CTRs contain information on the registry, while the surface rods are only sensitive to the oxide structure.

## High resolution core level spectroscopy measurements

The high resolution photoemission spectroscopy experiments have been performed at the I311 beamline [65] at the synchrotron radiation facility MAX-lab (Sweden) using undulator radiation in the energy range from 60 to 900 eV. The beamline and the experimental set-up were described in Chapter 3.

Oxidation experiments have been performed in the preparation chamber by exposing the CoGa(100) sample to different temperatures and partial oxygen pressures up to  $750^\circ\text{C}$  and  $5\times 10^{-5}$  mbar, respectively. After each oxidation step the sample was transferred in

the analysis chamber for performing the core level spectroscopy measurements. The Ga  $3d$  and O  $1s$  core level spectra were recorded after cooling the sample with liquid nitrogen in order to reduce the broadening induced by the thermal vibrations of the atoms in the crystal. The information depth has been varied either by changing the energy of the incident photons or by changing the detection angle. The spectra presented in this chapter were measured at normal emission angle (unless stated otherwise) and in a constant pass energy mode, which ensures a constant resolution throughout a whole spectrum. The pass energy refers to the kinetic energy an electron must possess in order to pass through the analyzer and be detected. The lower the pass energy, the higher the resolution of the spectrum.

## 6.3 Results and discussion

### 6.3.1 Structure of the surface gallium oxide

Detailed structural investigations of the surface gallium oxide on CoGa(100) surface have been initiated by Streitel *et al.* [96]. Within his work, SXRD measurements have been performed at the beamline ID32 at the ESRF. The photon energy was chosen to be 20 keV. For the surface structure determination, an oxide layer was prepared at 450°C and  $5 \times 10^{-7}$  mbar O<sub>2</sub>. A complete structural analysis of the oxide film was performed by the measurement of 16 symmetry inequivalent surface rods of the (2×1) superstructure and 4 independent crystal truncation rods, which contain information on the registry and distance of the overlayer with respect to the substrate (in total 850 independent structure factors). Based on the analysis of the x-ray diffraction data, a structural model for the surface oxide was initially proposed in [96]. The model showed deviations from the monoclinic  $\beta$ -Ga<sub>2</sub>O<sub>3</sub> bulk unit cell both in-plane and out-of-plane and had a thickness of 6.6 Å, which is about half of the height of a  $\beta$ -Ga<sub>2</sub>O<sub>3</sub> bulk unit cell. A layer of Ga atoms having a non-ionic bonding character was found at the substrate-oxide interface. Neglecting this layer, the stoichiometry of the ultra-thin film corresponds to the  $\beta$ -Ga<sub>2</sub>O<sub>3</sub> bulk oxide structure. The structural oxide model could describe very well the measured surface rods with a  $\chi^2$  of 0.94, but a less good agreement was found on the measured CTRs.

### 6.3.2 Searching for a new model

$\beta$ -Ga<sub>2</sub>O<sub>3</sub> exhibits a monoclinic structure and it is the only known thermodynamically stable bulk phase of Ga oxide. In addition, it has a very small mismatch to the CoGa

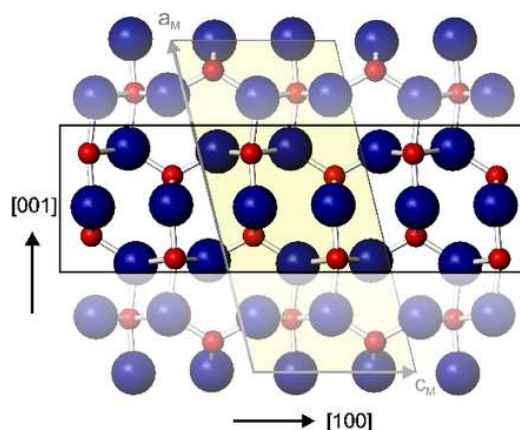


**Figure 6.5:** Bulk  $\beta$ -Ga<sub>2</sub>O<sub>3</sub> structure viewed along the [010] direction. The unit cell is marked by the yellow rectangle. The best fit to the data was achieved starting from the highlighted slab.

surface and is therefore a natural candidate for the structural refinement [98]. To find a starting model for the structure refinement, different slabs cut out of a Ga<sub>2</sub>O<sub>3</sub> bulk unit cell were considered and their calculated structure factor was compared to the x-ray data. First, the thickness of the oxide layer was determined by cutting slabs with different height out of the bulk Ga<sub>2</sub>O<sub>3</sub> crystal, such that the calculated structure factor matches the finite film thickness oscillation period on the surface rods. In the second step, all possible, differently terminated slabs with the same thickness were considered in the x-ray and DFT refinement. The best fit to the data was achieved starting from the slab highlighted in the Fig. 6.5.

Both Ga and Co substrate terminations have been considered. The structures have been relaxed and the configurations characterized by a DFT energy minimum are shown in Fig. 6.6(I-a) and (I-b)—*model I* (Ga-termination); (II-a) and (II-b)—*model II* (Co-termination). Fig. 6.7 shows the experimental x-ray diffraction structure factors (blue circles) as a function of the reciprocal lattice coordinate,  $L$ , perpendicular to the surface for different in-plane momentum transfers ( $H$ ,  $K$ ). A comparison with the the calculated structure factors for the DFT relaxed structures with Ga- (black lines) and Co- (red lines) termination with the experimental data, makes the poor agreement immediately apparent.

The *model III*—shown in Fig. 6.6(III-a) and (III-b)—has been obtained by removing one oxygen-ion from the interfacial layer. The stoichiometry of this oxide layer is Ga<sub>4</sub>O<sub>5</sub>, different than that of the stable bulk  $\beta$ -Ga<sub>2</sub>O<sub>3</sub>. However, the agreement between the experimental (blue symbols) and calculated (green lines) structure factors proved to be still very poor, as can be seen in Fig. 6.7. In addition, Ga  $3d^{1/2}$  and O  $1s$  core level shifts including final state effects have been calculated for the model III. The results of

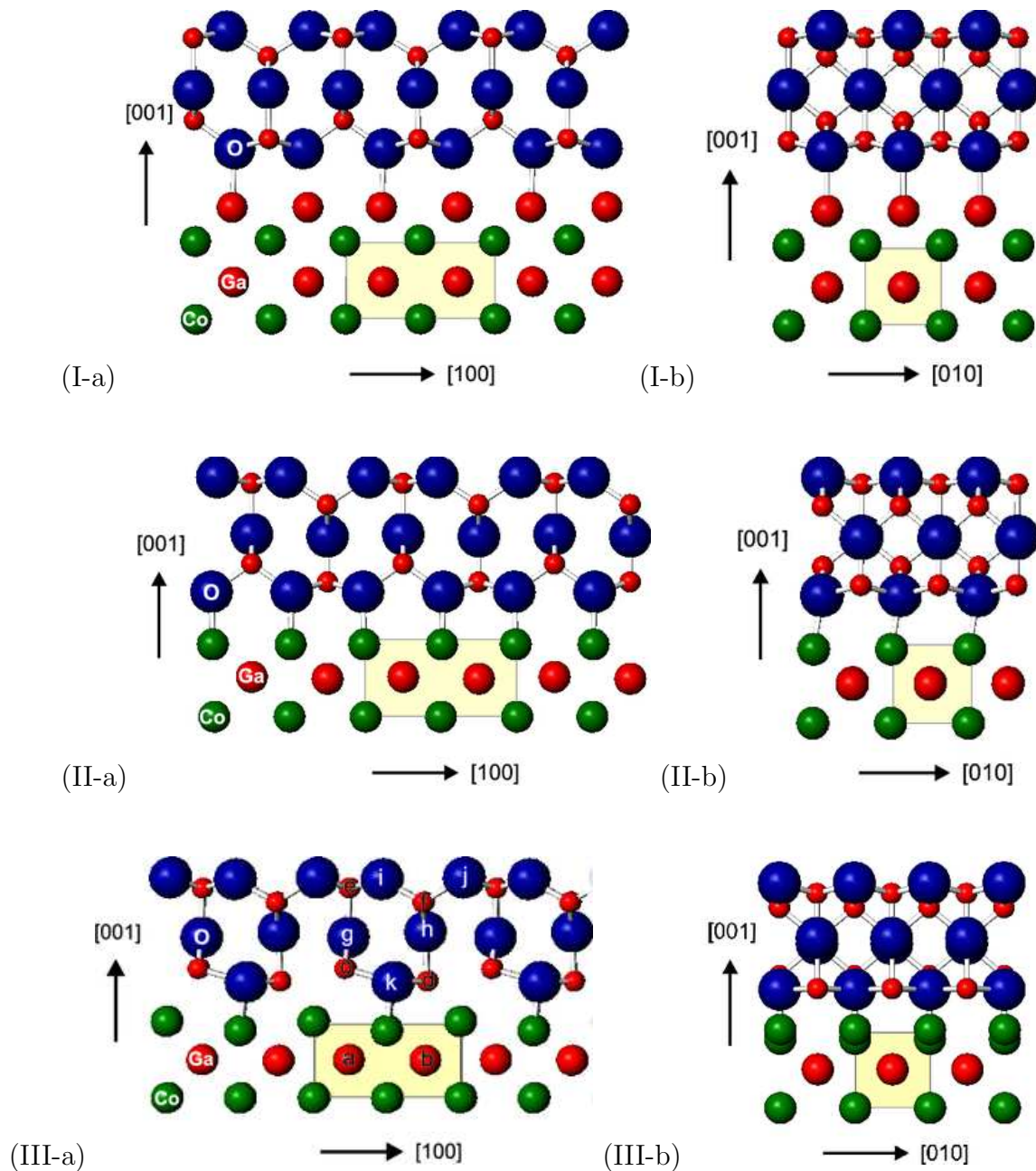


**Figure 6.6:** View of the tested models I, II and III along the [010] (left panel) and the [100] (right panel) direction of the substrate.

the calculations are shown in Fig. 6.8 (horizontal green lines) together with the values determined experimentally (blue symbols)<sup>4</sup>. In this figure, “III” indicates the calculated final state shifts and “E” marks the experimentally observed shifts. For Ga [Fig. 6.8(a)], the core level shifts are referred to the binding energy of the Ga atoms in the substrate, whereas in the case of O 1s [Fig. 6.8(b)] the peaks are aligned with respect to the lower

<sup>4</sup>The experimental Ga 3d and O 1s core level spectra are presented and discussed in more details in the next section.

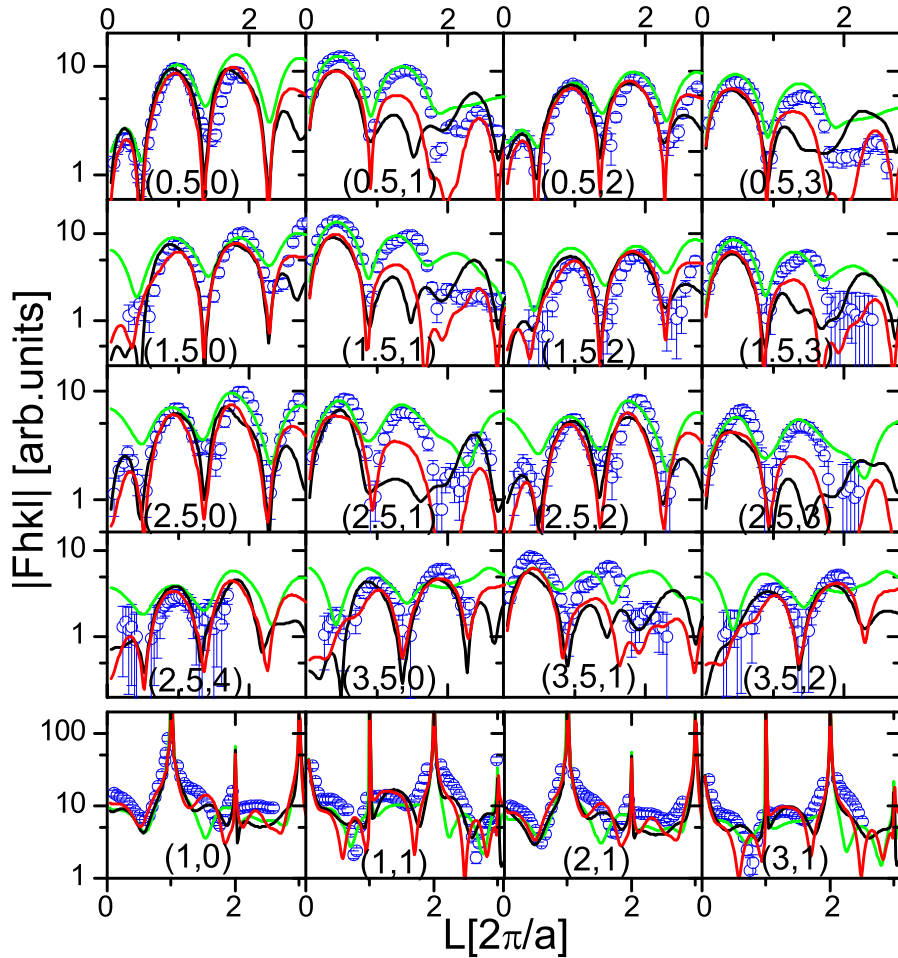


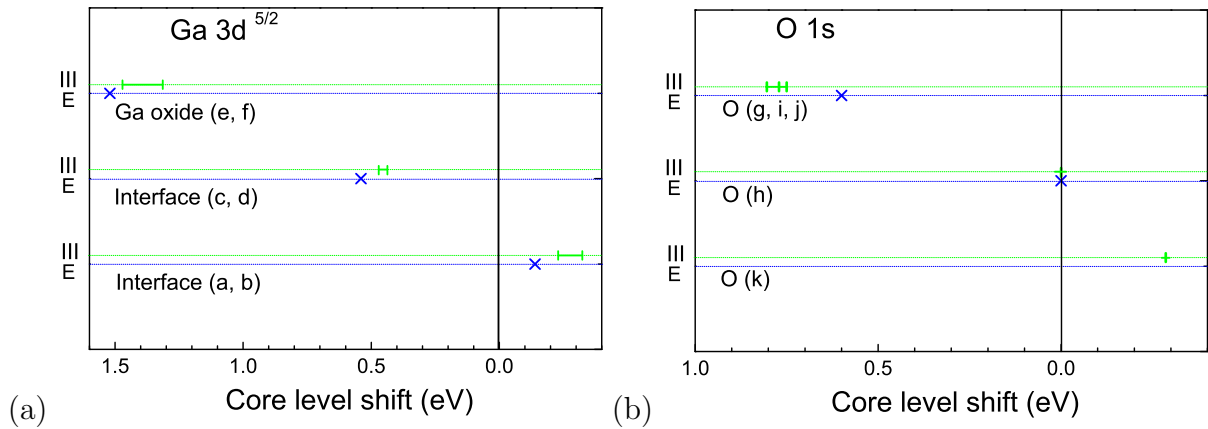
**Figure 6.7:** Experimental x-ray diffraction structure factors (blue symbols) as a function of the reciprocal lattice coordinate,  $L$ . For comparison the structure factors calculated from the model I (black), model II (red) and model III (green) are shown.

binding energy component in the experimental spectra. The poor agreement observed between both the experimental and calculated structure factors and the core level shifts renders this model unfavorable.

### New model of the surface gallium oxide

#### - SXR and DFT

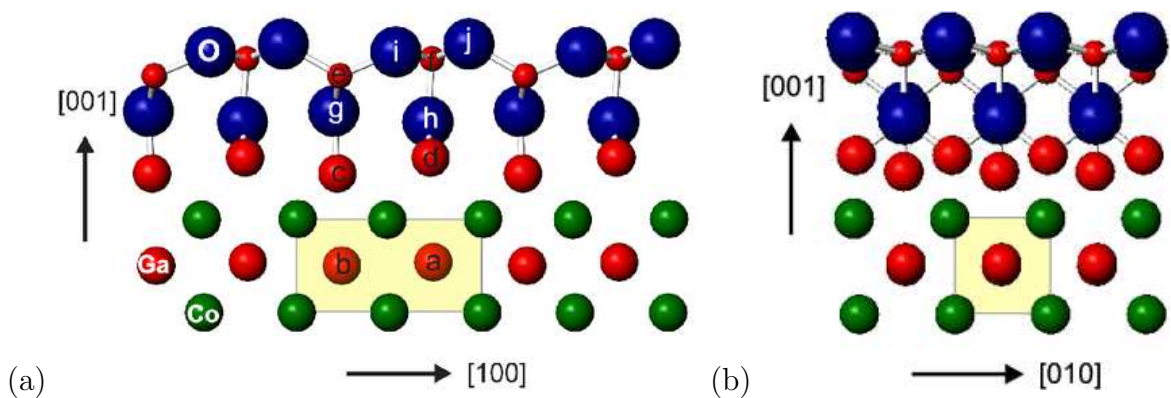
The best fit to the data was achieved for the structural model shown in the Fig. 6.9(a) and (b). The starting structure was derived from the model III by removing from the interface the oxygen ion labeled “k” in the Fig. 6.6(III-a). The structural model consists of an fcc-like oxygen ion double layer with Ga ions occupying octahedral and tetrahedral sites, which is the key structural element of  $\beta$ -Ga<sub>2</sub>O<sub>3</sub>. At the interface, the Ga ions occupy sites that follow the Ga<sub>2</sub>O<sub>3</sub> bulk sequence. The stoichiometry of the oxide layer is Ga<sub>4</sub>O<sub>4</sub>.



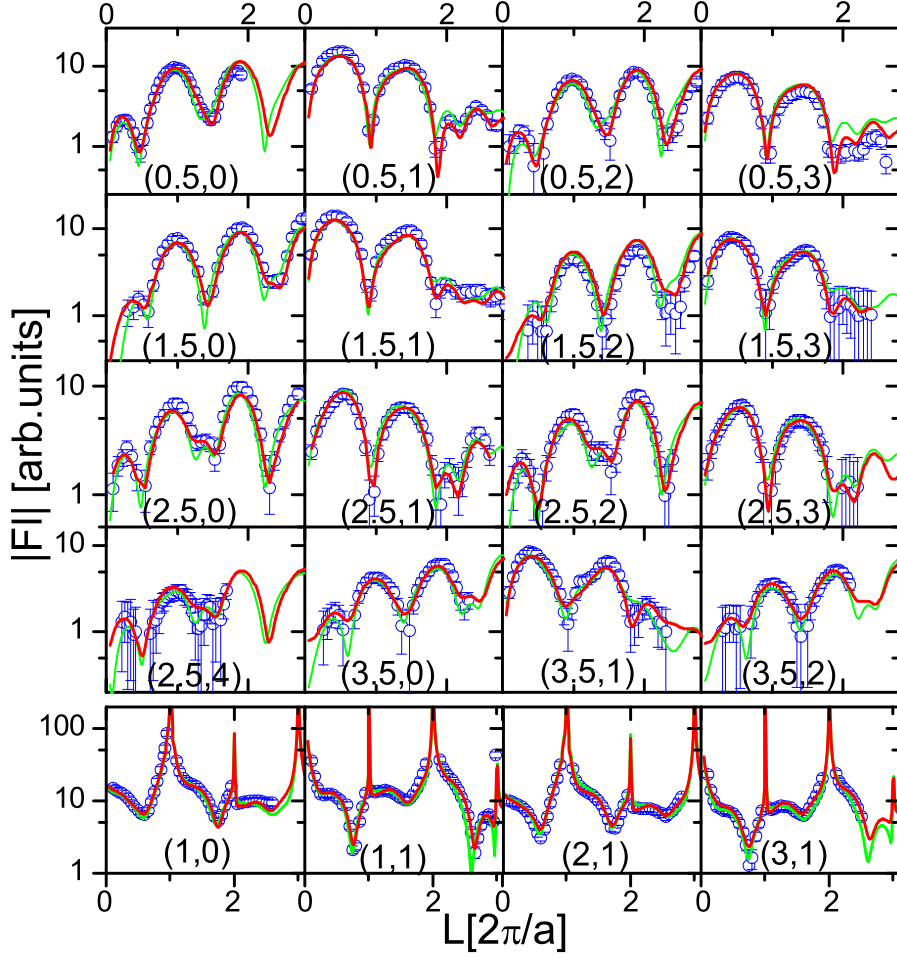
**Figure 6.8:** Comparison between the experimental (“E”, blue symbols) and theoretical (“III”, green horizontal lines) (a) Ga  $3d^{5/2}$  and (b) O  $1s$  core level shifts.

Fig. 6.10 shows the set of x-ray structure factors (blue symbols) together with the best fit yielding a  $\chi^2$  value of 1.05 (red curves). For the fit, an equal distribution of  $(2 \times 1)$  and  $(1 \times 2)$  domains, as well as mirror domains due to the monoclinic structure were included. In addition, the structure factors calculated for the relaxed DFT model are plotted in Fig. 6.10 (green curves), exhibiting a remarkably good agreement between theory and experiment. The relative deviations between the x-ray and DFT atomic coordinates within the oxide film are plotted in Fig. 6.11. The atomic coordinates for both the experimental and the DFT model of the surface gallium oxide are listed in the Appendix A. Because of the low x-ray scattering contrast between Co and Ga, it is not possible to distinguish between Co or Ga termination at the interface from the fit of the x-ray data. However, the DFT relaxed structure with Co termination is energetically less favorable than the one with Ga termination.

- HRCLS



**Figure 6.9:** Best fit model viewed along the (a)  $[010]$  and the (b)  $[100]$  direction of the substrate.



**Figure 6.10:** Experimental x-ray diffraction structure factors (blue symbols) as a function of the reciprocal lattice coordinate,  $L$ , for different in-plane momentum transfers. The structure factors calculated for the best fit structure (red curves) and for the most stable DFT model (green curves) are shown for comparison.

Additional confirmation for the correctness of the structural model is obtained from the Ga  $3d$  and O  $1s$  core level spectra. The spin-orbit interaction splits each Ga  $3d$  peak into a doublet. The higher angular momentum state ( $j=\frac{5}{2}$ ) lies higher in energy than the lower angular momentum state ( $j=\frac{3}{2}$ ), therefore the  $3d^{5/2}$  component appears at lower binding energies (18.54 eV). The theoretical intensity ratio between the doublet components is 3:2. In the case of  $3d$  level of Ga the spin-orbit splitting is 0.45 eV.

The Ga  $3d$  spectrum measured at 60 eV from the clean CoGa(100) surface is shown in Fig. 6.12. The decomposition of the core level spectra has been made using the FitXPS program written by D. L. Adams [58]. No surface core level shift could be observed within the experimental resolution. The lineshape of individual components consists of a Doniach-Šunjić profile [57] convoluted with a Gaussian distribution. A parabolic background was included in the fit. For an ordinary fitting procedure the fit parameters are

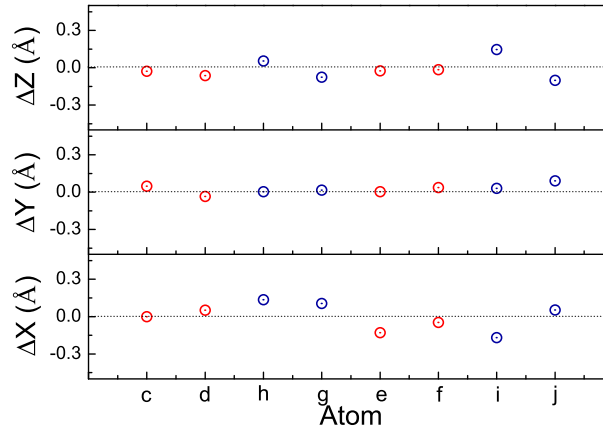


**Figure 6.11:** Relative deviation between the atomic coordinates in the DFT and experimental gallium oxide model. The red and blue symbols refer to gallium and oxygen ions, respectively.

the intensity, the binding energy (B.E.), the lineshape parameters (Lorentzian FWHM  $\Gamma$ , Gaussian FWHM  $\sigma$  and the asymmetry parameter,  $\alpha$ ) and the background parameters. Additional details about the fitting procedure have been given in Chapter 3. In Fig. 6.13(a) the Ga  $3d$  core level spectrum of the oxidized sample measured at a photon energy of 150 eV is shown. In order to obtain a full coverage of the substrate surface, the surface gallium oxide layer was prepared by oxidation at 450°C and 1000 L O<sub>2</sub> ( $10^{-5}$  mbar O<sub>2</sub> for 100 s.) The decomposition of the spectrum reveals four different components. The Ga  $3d^{5/2}$  component at 18.54 eV (green) is attributed to the Ga atoms residing in the CoGa substrate. The other three components (orange, blue, red) are oxygen-induced and the assignment to different Ga ions is presented further below. The O  $1s$  spectrum recorded at 700 eV photon energy is shown in Fig. 6.13(b). Two different components split by 0.6 eV could be identified. The fit parameters of the Ga  $3d$  and O  $1s$  spectrum are presented in Appendix B.

DFT-based calculations of the Ga  $3d$  and O  $1s$  core level shifts have been performed

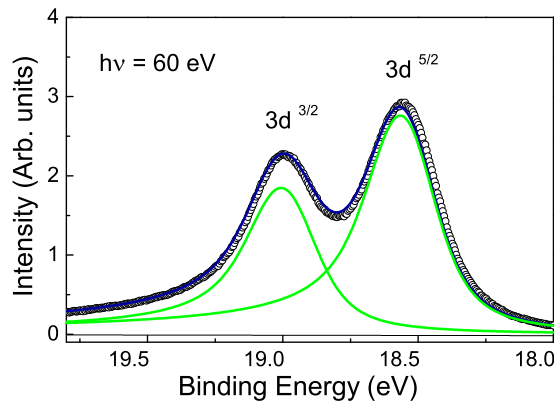


**Figure 6.12:** Ga  $3d$  spectrum of the clean CoGa(100) surface.

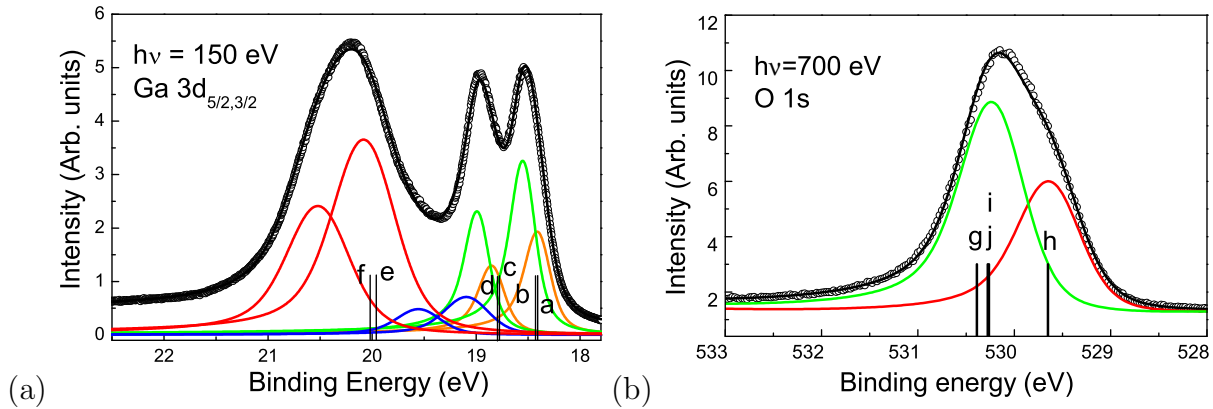


**Figure 6.13:** The decomposition of the (a) Ga  $3d$  and (b) O  $1s$  core level spectra of the surface gallium oxide.

both in initial and final state approximation. In the initial state approximation, one core electron is excited and the electronic screening of the core hole is totally neglected (no relaxation of the surrounding electrons are allowed). It is however important to include the final states effects, therefore the relaxation of the electrons is permitted within the final state approximation. The calculated Ga  $3d$  and O  $1s$  core level shifts (including final state effects) for the fully relaxed DFT structure with Ga interfacial termination are in good agreement with the experimental core level spectra. The positions of the calculated core level components for both Ga  $3d$  and O  $1s$  are marked by the black vertical lines in Fig. 6.13. For Ga  $3d$  the bulk-level is employed to align the theoretical and experimental spectra. For O  $1s$  the lowest-energy theoretical peak is simply aligned to the lowest-energy experimental peak.

The Ga atoms labeled “a” and “b” in Fig. 6.9(a) exhibit a core level shift of 0.15 eV towards lower binding energies. A similar behavior was reported for the photoemission spectra of the oxidized Al(111) [55]. The shift to lower binding energies was attributed to the final-state effects of core-hole screening: these atoms are located at the interface without being directly bound the oxygen ions, being therefore less screened than the bulk Ga atoms, which leads to a core level shift towards lower binding energies. For atoms “c” and “d” (“e” and “f”) a chemical shift of 0.54 eV (1.53 eV) to higher binding energies is observed. Oxygen ions labeled “g”, “i” and “j” have a similar binding energy, whereas atom “h” possesses a lower binding energy ( $-0.6$  eV), giving rise to the experimentally observed two component lineshape of the O  $1s$  level.

In general, the escape depth follows the kinetic energy of the outgoing photoelectron according to the “universal curve” as discussed in Chapter 3. Therefore, the relative depth of the photo-emitting atoms can be probed by recording spectra at different incident

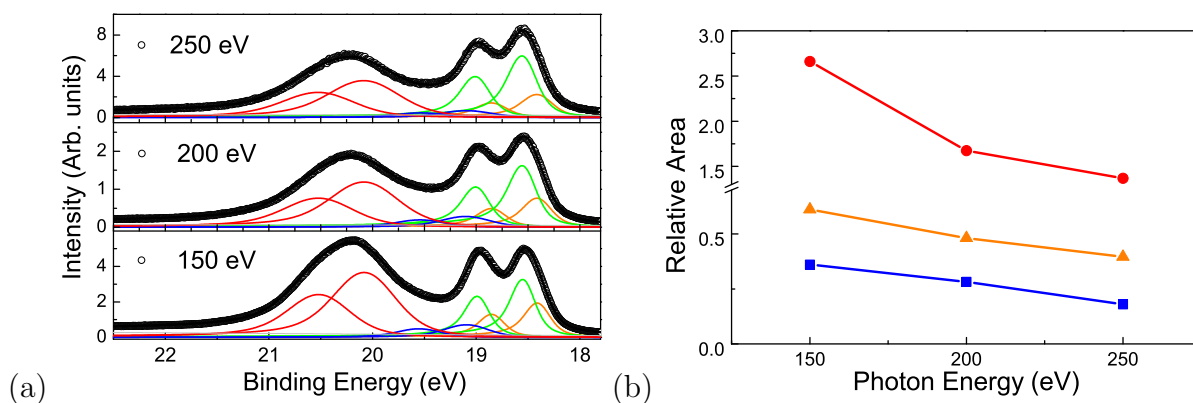


**Figure 6.14:** (a) Ga 3d spectra as a function of incident photon energy measured after oxidation at 450°C with 1000 L O<sub>2</sub>. (b) The relative area of the oxygen-induced components with respect to the bulk component as a function of photon energy.

photon energies. In Fig. 6.14(a), the Ga 3d core level spectra measured at different photon energies, i. e., 150 eV, 200 eV and 250 eV, are shown. The relative area of the oxygen-induced Ga 3d<sup>5/2</sup> components (orange, blue, red) with respect to the bulk Ga 3d<sup>5/2</sup> component (green) as a function of the incident photon energy is shown in Fig. 6.14(b). The most pronounced decrease with increasing the photon energy was observed for the highest binding energy component (red), implying that the photo-emitting atoms are located close to the surface. This observation is in agreement with the proposed model and the DFT-calculated core level shift: this component is attributed to the “e” and “f”-type of Ga ions, which form the topmost Ga layer in the proposed structural model.

### Surface oxide stability as a function of oxygen exposure

The stability of the surface oxide as a function of oxygen exposure at 450°C was investigated by means of HRCLS measurements. Experimentally, it was observed that the structure of the surface oxide does not change as the oxygen exposure was increased from 1 L to 5000 L. This is illustrated in Fig. 6.15 by the Ga 3d and O 1s spectra measured after different oxygen exposures at 450°C. The partial oxygen pressure and the oxidation time for each individual oxidation measurements are presented in Table 6.2. The dotted lines in Fig. 6.15(a) mark the binding energies of the Ga 3d<sup>5/2</sup> components as obtained from the deconvolution of the Ga 3d spectrum measured after 1000 L oxygen exposure [see Fig. 6.13(a)]. Two components shifted by 0.6 eV have been used for the deconvolution of the O 1s spectra shown in Fig. 6.15(b). In order to estimate the oxide coverage, the relative area of the O 1s components for different exposures with respect to the area of the O 1s component at 1000 L oxygen exposure was calculated. By comparison with the spectra measured after 5000 L oxygen (not shown), it could be concluded that a full oxide

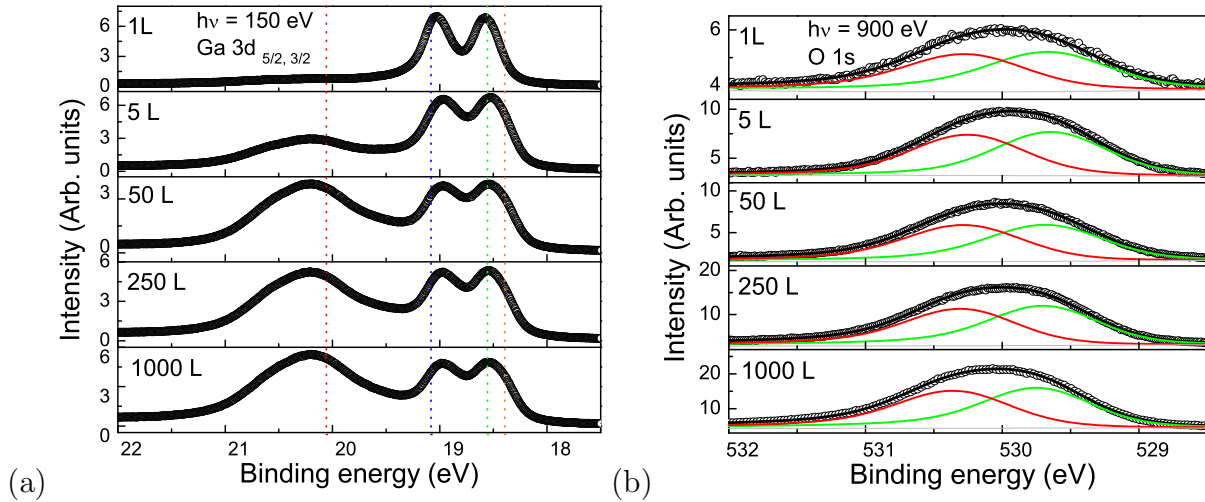


**Figure 6.15:** (a) Ga 3*d* and (b) O 1*s* spectra recorded after different oxygen exposures at 450°C.

coverage is already reached after exposure to 1000 L oxygen. The values are listed in the last column of Table 6.2.

**Table 6.2:** The partial oxygen pressure and the oxidation time for each individual oxidation experiment. The last column indicates the coverage estimated from the O 1*s* core level spectra.

Oxygen exposure	$p_{O_2}$ [mbar]	Time [s]	Relative area
1 L	$10^{-8}$	100	0.14
5 L	$5 \times 10^{-8}$	100	0.36
50 L	$5 \times 10^{-7}$	100	0.40
250 L	$10^{-6}$	250	0.76
1000 L	$10^{-5}$	100	1.00

Increasing the oxidation temperature to 620°C and dosing 1000 L oxygen ( $10^{-5}$  mbar for 100 seconds) resulted again in no change in the Ga 3*d* and O 1*s* core level spectra, as shown in Fig. 6.16 [for comparison, see Fig. 6.13]. Similar values of the Ga 3*d* and O 1*s* fit parameters are indicative of an unchanged surface oxide structure. Decreasing the take-off angle by 10° to vary the escape depth of the emitted photoelectrons, led to a significant decrease of the lower binding energy component in the O 1*s* spectra, as can be observed in Fig. 6.16(b), meaning that the photo-emitting ions are located deeper in the oxide. The proposed model is in agreement with this observation.

### 6.3.3 ( $p$ - $T$ )–dependent surface oxide growth

Having proposed a structural model for the ultra-thin gallium oxide, the next step was to investigate the onset of its formation as a function of the oxygen partial pressure and temperature. *In situ* surface x-ray diffraction measurements have been performed in order to investigate the onset of surface oxide formation at different oxidation temperatures ranging from 650°C to 770°C. The results presented in this section have been collected during the ANKA1 beamtime.

The oxidation experiments have been performed as follows: the CoGa(100) crystal was first heated at the oxidation temperature and oxygen was introduced in the portable diffraction chamber while the intensity was followed in real time on an oxide-sensitive reciprocal space position. If no oxide growth was to be observed, the oxygen was pumped off and a higher pressure was successively applied until signal from the oxide was detected. As an example, the timescan on the (0, 0.5, 0.96) oxide peak measured during oxidation at 670°C with  $3 \times 10^{-7}$  mbar  $O_2$  is shown in Fig. 6.17(a). A very rapid oxide growth was observed. However, decreasing the oxygen pressure to  $10^{-7}$  mbar caused the intensity to drop down, revealing the instability of the oxide at lower oxygen pressures.

In Fig. 6.17(b) rocking scans through the (0, 0.5, 0.96) oxide peak are shown for three different oxidation conditions: after applying  $10^{-7}$  mbar of oxygen (filled blue circles), after oxidation at  $3 \times 10^{-7}$  mbar  $O_2$  (open black squares) and after decreasing the pressure from  $3 \times 10^{-7}$  to  $10^{-7}$  mbar  $O_2$  (open blue circles). A slight broadening of the peak took place after decreasing the oxygen pressure to  $10^{-7}$  mbar  $O_2$ . The diffraction signal along the (0.50 $L$ ) reciprocal lattice direction is presented in Fig. 6.17(c) for the above mentioned oxidation conditions. Apart from the decrease in intensity at lower oxygen pressures associated with a lower oxide coverage, no significant changes were observed. Similar

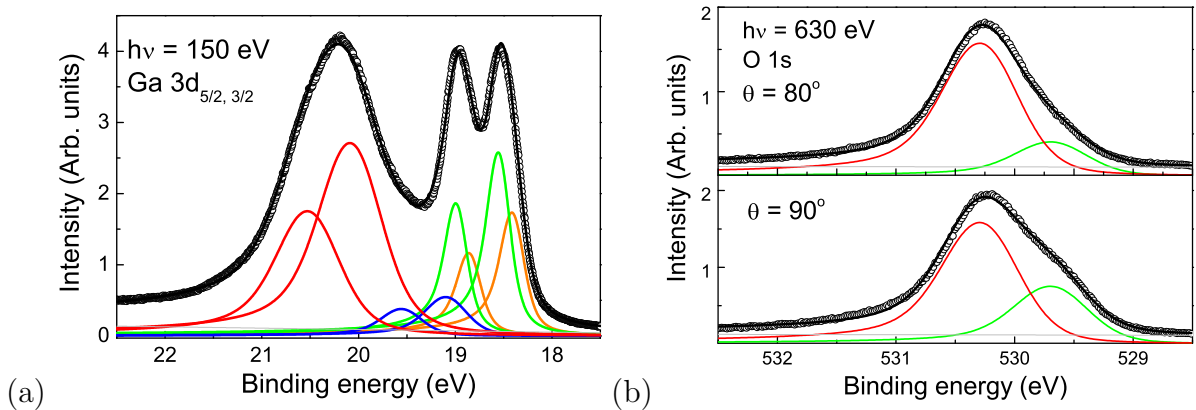


**Figure 6.16:** Ga 3d (a) and O 1s (b) spectra after oxidation at 620°C.

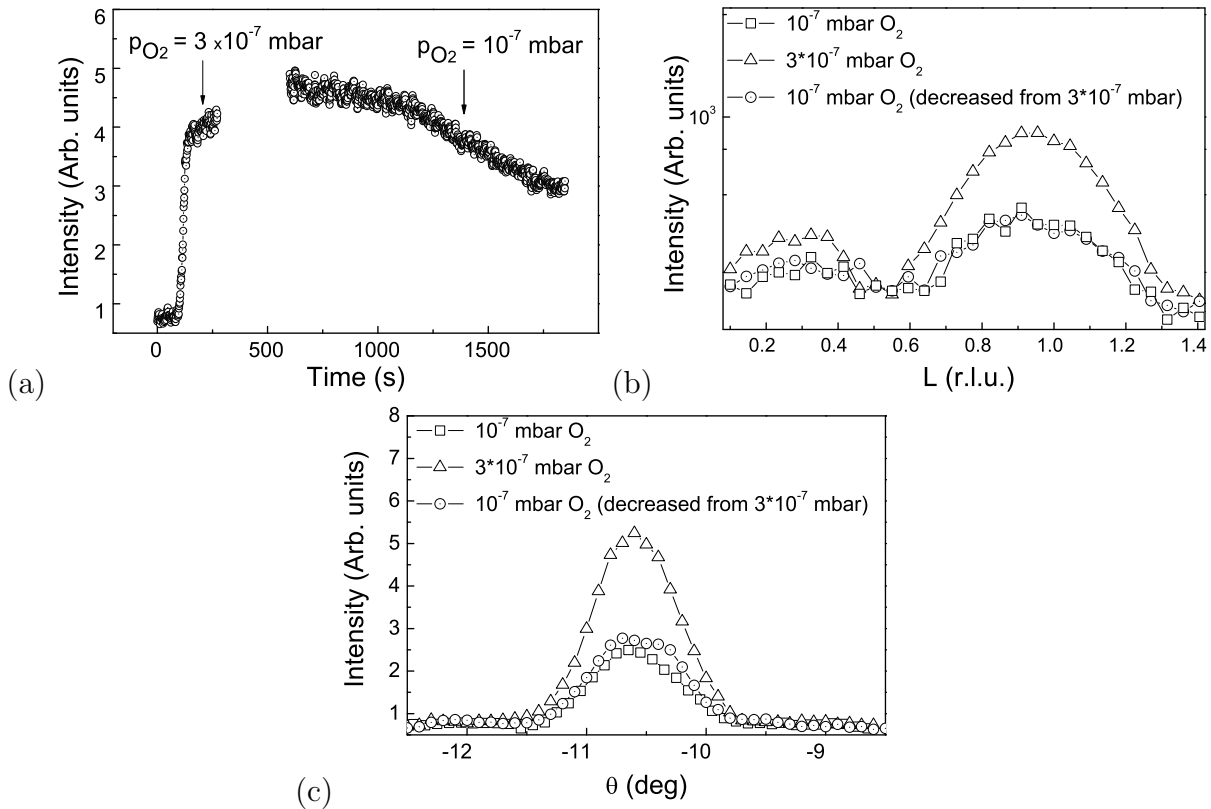


**Figure 6.17:** (a) Timescan on (0, 0.5, 0.96) position measured during oxidation at 670°C with  $3 \times 10^{-7}$  mbar  $O_2$ . (b) Diffracted intensity along the (00.5L) reciprocal lattice direction. (c) Rocking scan on the (0, 0.5, 0.96) oxide peak.

experiments have been conducted at several temperatures up to 770°C. The observed conditions for the onset of the oxide growth are summarized in Table 6.3.

### 6.3.4 Transition of the surface oxide to bulk $Ga_2O_3$

Significantly higher oxygen pressures at relatively high temperatures facilitate the formation of bulk oxide films. *In situ* SXRD measurements have been performed in order to

**Table 6.3:** The ( $p$ - $T$ ) conditions for the onset of the surface oxide growth.

Temperature [°C]	Partial oxygen pressure [mbar]
670	$10^{-7}$
690	$3 \times 10^{-7}$
700	$3 \times 10^{-7}$
740	$8 \times 10^{-7}$
770	$2.5 \times 10^{-6}$

study under which conditions (oxygen pressure and temperature) the surface oxide starts to transform to a bulk oxide. The results presented in this section have been collected during the ANKA2 beamtime. The experiments have been performed as follows: first, the surface oxide layer has been prepared by oxidation at 450°C and  $2 \times 10^{-7}$  mbar oxygen. In the next step, its stability was tested by applying oxygen at different pressures while the sample was held at temperatures between room temperature and 650°C. Synchronously, the structural changes in the oxide layer were followed by monitoring the intensity on a bulk oxide sensitive reciprocal space position [e.g., (0.5, 0, 1.08)]. In the next paragraph, the reciprocal lattice of  $\beta$ -Ga<sub>2</sub>O<sub>3</sub> is described in order to facilitate the understanding of the diffraction data subsequently presented.

### A. Reciprocal lattice of $\beta$ -Ga<sub>2</sub>O<sub>3</sub>

$\beta$ -Ga<sub>2</sub>O<sub>3</sub> has a monoclinic structure which was previously discussed in Chapter 3. The lattice constants of  $\beta$ -Ga<sub>2</sub>O<sub>3</sub> are:  $a_M=1.223$  nm,  $b_M=0.304$  nm,  $c_M=0.58$  nm and  $\alpha=90^\circ$ ,  $\beta=103.7^\circ$ ,  $\gamma=90^\circ$ .  $b_M$  possesses a misfit of 5.5% and  $\frac{c_M}{2}$  a misfit of 0.7% with respect to the CoGa (100) substrate with  $a_C=0.2878$  nm, opening up the possibility of epitaxial growth<sup>5</sup>.

The monoclinic  $b_M$ - and  $c_M$ -axis lay in the surface plane and are oriented parallel to the CoGa (010) and (100) directions, respectively, building up the (2×1) superstructure. Because of the four-fold symmetry of the substrate surface also (1×2) oxide domains may exist, that possess their own set of superstructure rods. The monoclinic  $a_M$ -axis is tilted by 14° with respect to the surface normal and two types of out-of-plane domains for each in-plane domain exist: the oxide unit cell can be rotated by 180° around the surface normal still fulfilling the epitaxial relationships described above. For each of the out-of-plane domains the reciprocal space  $a_M^*$ -axis is perpendicular to the surface, as it is depicted in Fig. 6.18. As a consequence, the reciprocal space  $c_M^*$ -axis is no longer parallel to the surface and for one type of domains the  $c_M^*$ -axis will point into the surface (red) and for the other type of domains out of the surface (black). This leads to an overlapping of oxide reflections in the direction perpendicular to the surface. Along the (0.50L) substrate reciprocal lattice direction, reflections from both (2×1) mirror domains contribute at different perpendicular momentum transfers. This appears as a splitting of the reflections along the (0.50L) rod. The bulk oxide reflections were indexed within the monoclinic coordinates. The monoclinic (0, 0, 1) reflection from the first type of domains occurs at  $L \neq 0$ , because  $c_M^*$  is not laying in the surface plane. The equivalent (0, 0,  $\bar{1}$ )

<sup>5</sup>In this section, the 'M' and 'C' subscripts are used to denote the monoclinic and the cubic coordinates, respectively.

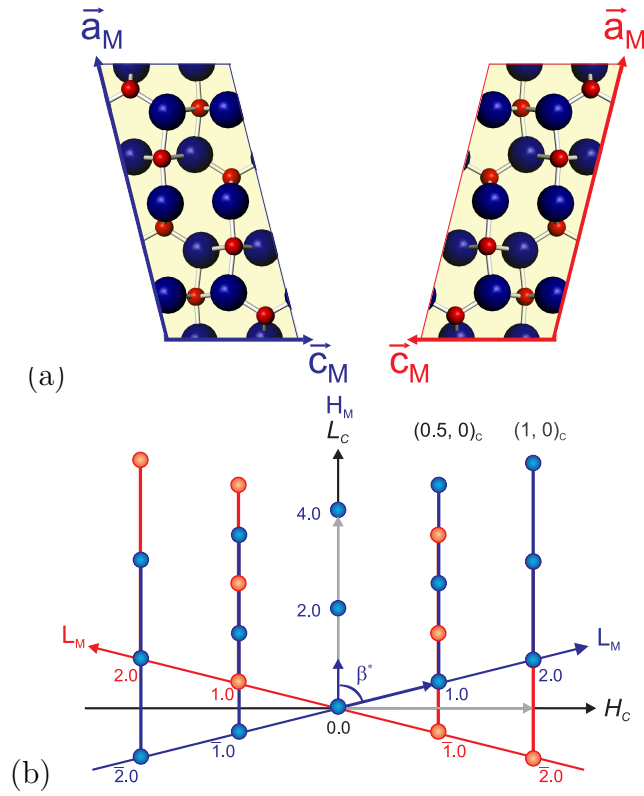


**Figure 6.18:** View of the (a) real and (b) reciprocal space  $\beta$ -Ga<sub>2</sub>O<sub>3</sub> lattice illustrating the two out-of-plane domains.

reflection from the second type of domains is laying below the surface and cannot be measured. All other reflections are split, according to the two out-of-plane domains. Assuming a perfect  $(2 \times 1)$  registry with the substrate and choosing the  $c_C$  axis to be perpendicular to the surface, the monoclinic coordinates may be transformed into cubic coordinates compatible to those of CoGa substrate according to:

$$\begin{aligned} a_M &= -r_2 a_C + r_1 c_C \\ b_M &= b_C \\ c_M &= 2a_C, \end{aligned} \quad (6.1)$$

where  $r_1=4.12325$  is the projection of the  $a_M$  axis on the  $c_C$  axis and  $r_2=0.5140$  is the projection of  $a_M$  on the cubic  $a_C$  axis. The correspondence between some of the oxide reflections indexed in monoclinic and cubic coordinates is given in Table 6.4.

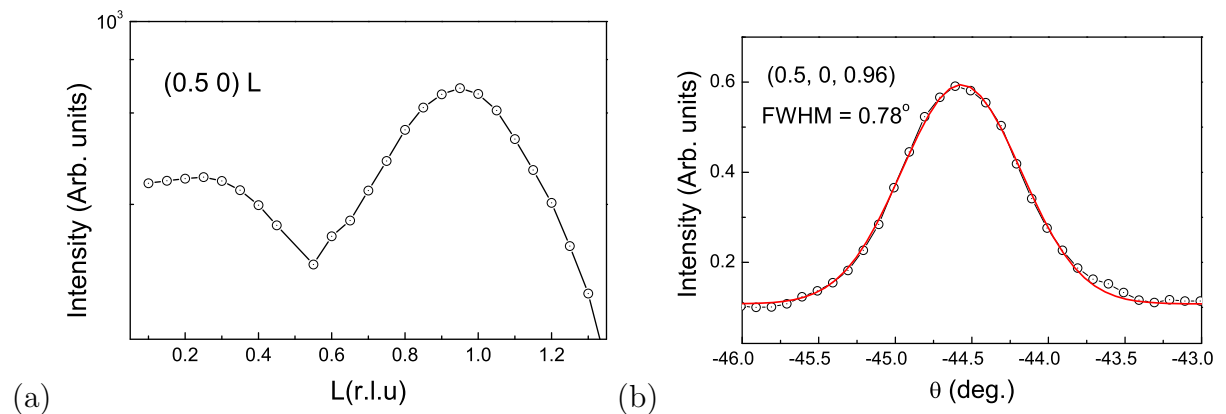
## B. Surface oxide stability at room temperature

Fig. 6.19(a) shows the diffracted intensity along the  $(0.50L)$  reciprocal lattice direction measured after exposing the surface oxide layer at 1 bar of oxygen at room temperature for 90 minutes. No increase in the width of the rocking scan on the  $(0, 0.5, 0.96)$  reciprocal

**Table 6.4:** The correspondence between the monoclinic and cubic coordinates for some of the oxide reflections arising from the  $(2 \times 1)$  in-plane domains.

Monoclinic coordinates	Cubic coordinates
$(0, 0, \bar{1})$	$(0.5, 0, -0.11)$
$(0, 0, 1)$	$(0.5, 0, 0.13)$
$(2, 0, \bar{1})$	$(0.5, 0, 0.37)$
$(2, 0, 1)$	$(0.5, 0, 0.61)$
$(4, 0, \bar{1})$	$(0.5, 0, 0.85)$
$(4, 0, 1)$	$(0.5, 0, 1.09)$
$(6, 0, \bar{1})$	$(0.5, 0, 1.33)$
$(6, 0, 1)$	$(0.5, 0, 1.57)$

space position was observed (scan not shown here). Apart from a slight decrease in the scattered intensity along the surface rods, oxygen exposure at room temperature did not cause any significant changes of the surface oxide even at partial pressures as high as 1 bar  $O_2$ . Our experimental observations show that for temperatures lower than  $350^\circ\text{C}$ , bulk oxide formation is kinetically hindered. Even if—according to thermodynamical considerations—a bulk oxide phase would be predicted at this conditions of temperature and partial oxygen pressure, further growth of the oxide layer is limited by two factors: oxygen dissociation—the surface oxide forms an oxygen-terminated closed layer—and by the diffusion of Ga from the substrate. Therefore, higher temperatures and oxygen pressures are needed in order to activate the thermal diffusion of ions and to create defect

**Figure 6.19:** (a) Diffracted intensity along the  $(0.50L)$  reciprocal lattice direction. (b) Rocking scan on the  $(0, 0.5, 0.96)$  oxide peak after exposing the surface oxide layer at 1 bar of oxygen at room temperature.

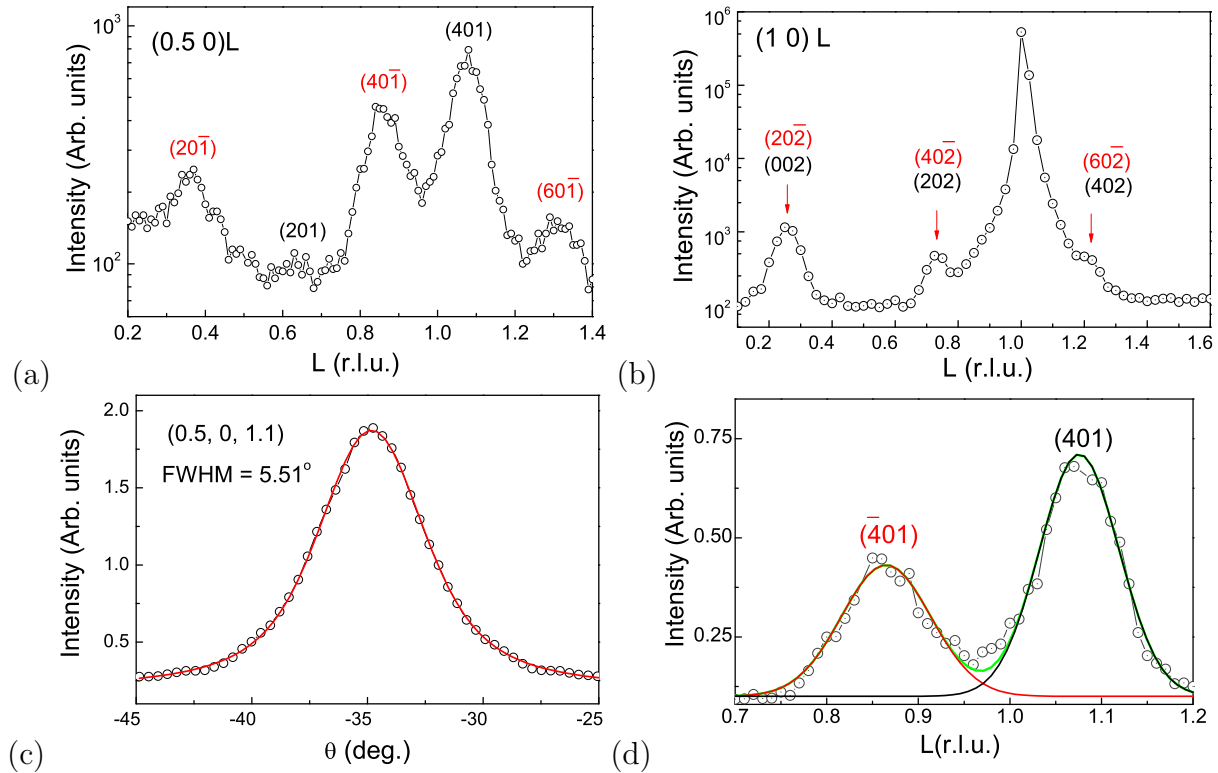


**Figure 6.20:** Bulk oxide formation at 450°C and 1 mbar O<sub>2</sub>: (a) Diffracted intensity along the  $(0.50L)$  reciprocal lattice direction. (b) Diffracted intensity along the  $(10L)$  reciprocal lattice direction. (c) Rocking scan on the  $(0.5, 0, 1.1)$  oxide peak. (d) The  $(4, 0, 1)_M$  and  $(4, 0, \bar{1})_M$  oxide reflections. Each of the peaks was fitted to a Lorentzian lineshape.

sites for oxygen dissociation, so that the growth of the existing layer can proceed further. At 350°C, after one hour exposure at 0.1 bar O<sub>2</sub>, the formation of very thin bulk oxide islands was observed [scan not shown here].

### C. Oxidation at 450°C

The observed diffraction signal along the  $(0.50L)$  reciprocal space direction changed significantly as the temperature has been increased and 450°C, respectively. After 10 minutes exposure at 1 mbar O<sub>2</sub>, several peaks appeared at  $L=0.37, 0.61, 0.85, 1.09$  and  $1.33$  along the  $(0.50L)$  rod, as can be observed in Fig. 6.20(a). These reflections arise from the bulk-like diffraction from an epitaxial  $\beta$ -Ga<sub>2</sub>O<sub>3</sub> oxide. They were labeled according to the monoclinic coordinate system (see section 6.3.4.A. for details). They appear at non-integer  $L$ -values, due to the fact that for the diffraction measurements the reciprocal lattice was defined with respect to the cubic coordinate system of the CoGa substrate.

The out-of-plane diffraction signal along the reciprocal  $(10L)$  direction is shown in Fig. 6.20(b). In addition to the  $(1, 0, 1)$  Bragg peak of the substrate, several other oxide

**Table 6.5:** FWHM of the oxide reflections from the rocking scans.

Peak	$L$ (r.l.u.)	FWHM
$(2, 0, \bar{1})_M$	0.37	$3.52^\circ$
$(2, 0, 1)_M$	0.61	$7^\circ$
$(4, 0, \bar{1})_M$	0.85	$5.26^\circ$
$(4, 0, 1)_M$	1.08	$5.51^\circ$
$(6, 0, \bar{1})_M$	1.33	$6.94^\circ$

reflections are to be observed. Along this direction, the reflections from both  $(2 \times 1)$  out-of-plane domains of the oxide overlap. In Fig. 6.20(c) a rocking scan through the  $(0.5, 0, 1.1)$  oxide peak is shown (black symbols) together with the fit to the data points (red line). The increased value of the FWHM ( $\sim 5.5^\circ$ ) is indicative of either an enhanced mosaic spread or of a small domain size of  $\beta\text{-Ga}_2\text{O}_3$ . A similar value has been found also for the  $(0.5, 0, 0.85)$  reflection, as can be seen in Table 6.5.

Since no finite thickness oscillations were observed along the  $(0.50L)$  rod, the oxide surface must be rather rough. The measured width of the  $(4, 0, 1)_M$  and  $(4, 0, \bar{1})_M$  reflections in the  $(0.50L)$  scan indicate an average film thickness of 2.9 and 3.3 nm, respectively [cf Table 6.6]. The FWHM was determined by fitting the two peaks with Lorentz functions [Fig. 6.20(d)].

#### D. Oxidation at $500^\circ\text{C}$

At  $500^\circ\text{C}$  the surface oxide layer was found to be stable up to an oxygen pressure of  $10^{-2}$  mbar. In Fig. 6.21(a) the time evolution of the intensity on the  $(0.5, 0, 1.08)$  bulk oxide peak is shown. After 5 minutes at  $10^{-2}$  mbar a very small intensity increase was observed. A dramatically increase in the bulk oxide growth rate was obtained by raising the partial oxygen pressure to  $10^{-1}$  mbar. The bulk oxide grown in these conditions shows the same orientation relationship with the underlying substrate as the bulk oxide layer

**Table 6.6:** Average thickness of the oxide estimated from the FWHM of the  $(4, 0, 1)_M$  and  $(4, 0, \bar{1})_M$  oxide peaks after oxidation at  $450^\circ\text{C}$ .

Peak	$L$ (r.l.u.)	FWHM (r.l.u.)	Average thickness (nm)
$(4, 0, \bar{1})_M$	0.85	0.0978	2.9
$(4, 0, 1)_M$	1.08	0.0867	3.3

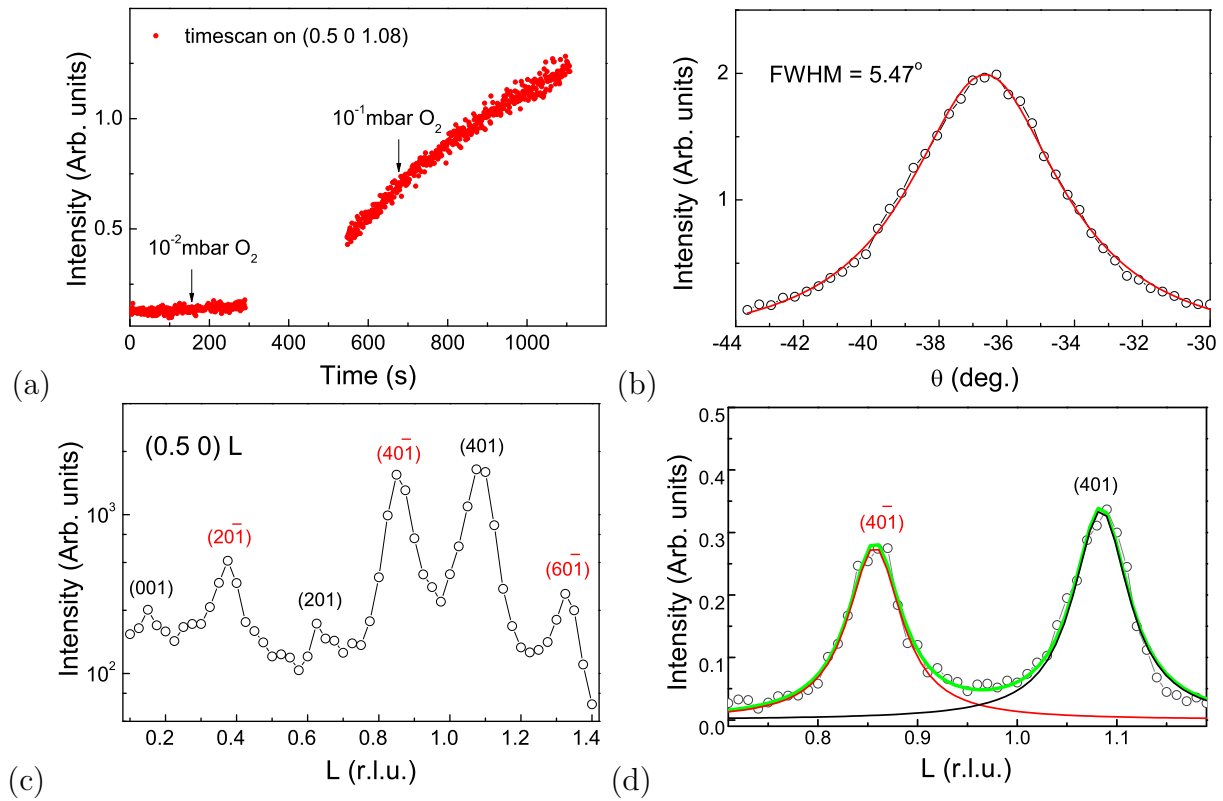


**Figure 6.21:** (a) Timescan on the  $(0.5, 0, 1.08)$  oxide peak during oxidation at  $500^\circ\text{C}$ . (b) Rocking scan on the  $(0.5, 0, 1.08)$  oxide peak after exposure at  $10^{-1}$  mbar  $\text{O}_2$ . (c) Diffracted intensity along the  $(0.50L)$  reciprocal lattice direction. (d) The  $(4, 0, 1)_M$  and  $(4, 0, \bar{1})_M$  oxide reflections. Each of the peaks was fitted to a Lorentz function.

formed at  $450^\circ\text{C}$ . A similar value of the FWHM of the  $(0.5, 0, 1.08)$  peak was estimated [Fig. 6.21(b)]. Fig. 6.21(c) shows the  $(0.50L)$  superstructure rod measured after exposure at  $10^{-1}$  mbar oxygen. The bulk oxide reflections were indexed in monoclinic coordinates. An average oxide thickness of 4.3–4.5 nm was estimated from the width of the  $(4, 0, 1)_M$  and  $(4, 0, \bar{1})_M$  bulk oxide peaks, respectively. A Lorentzian lineshape was used to describe the shape of the two peaks shown in Fig. 6.21(d). The FWHM together with the estimated thickness values are given in Table 6.7.

### E. Oxidation at $600^\circ\text{C}$ and $650^\circ\text{C}$

In a similar manner, the transition to the bulk  $\text{Ga}_2\text{O}_3$  was followed at 600 and  $650^\circ\text{C}$ . With increasing the oxidation temperature, the bulk oxide was found to form at lower partial oxygen pressures:  $5 \times 10^{-2}$  mbar  $\text{O}_2$  at  $600^\circ\text{C}$  and  $10^{-2}$  mbar  $\text{O}_2$  at  $650^\circ\text{C}$ . A faster oxide growth took place at  $650^\circ\text{C}$ . This can be observed by comparison of Fig. 6.22(a) and Fig. 6.23(a), where the time evolution of the intensity on the  $(0.5, 0, 1.08)$  oxide peak at  $600^\circ\text{C}$  and  $650^\circ\text{C}$ , respectively, is plotted. A decrease of the FWHM of the  $(0.5, 0, 1.08)$

**Table 6.7:** Average thickness of the oxide estimated from the FWHM of the  $(4, 0, 1)_M$  and  $(4, 0, \bar{1})_M$  oxide peaks after the oxidation at 500°C.

Peak	$L$ (r.l.u.)	FWHM (r.l.u.)	Average thickness (nm)
$(4, 0, \bar{1})_M$	0.85	0.0651	4.5
$(4, 0, 1)_M$	1.09	0.0679	4.3

peak [Fig. 6.22(b) and Fig. 6.23(b)] is indicative of a better ordered oxide compared to the oxide grown at 450°C and 500°C. The average oxide thickness—estimated as described before from the width of the  $(4, 0, 1)$  and  $(4, 0, \bar{1})$  reflections [cf Fig. 6.22(d) and Fig. 6.23(d)]—was determined to be 9 and 12 nm for the 600°C and 650°C oxidation, respectively [Table 6.8]. *Ex situ* Atomic Force Microscopy (AFM) measurements have been performed in order to study the morphology of the bulk oxide grown at 650°C. Fig. 6.24(a) shows an AFM image measured in contact mode. It can be observed that the growth of the bulk oxide islands takes places preferentially along two directions perpendicular to each other, that correspond to the  $[100]$  and  $[010]$  substrate directions. The oxide surface is rough, in agreement with the x-ray observations. The two line profiles in Fig. 6.24(b) reveal the presence of oxide islands of different heights up to  $\sim 30$  nm. Following the three-dimensional growth mode of the bulk oxide, islands characterized by a wide range of height distribution coexist, which causes the finite thickness oscillations in the x-ray diffraction data to cancel out.

### 6.3.5 Bulk $\text{Ga}_2\text{O}_3$ growth at high temperature

Fig. 6.25(a) and (b) show the development of the experimental Ga  $3d$  and O  $1s$  core level spectra for the sequence of oxides formed on the CoGa(100) surface at increasingly higher temperatures and the oxygen exposures. The particular oxidation conditions are indicated on each graph. The topmost panels present the Ga  $3d$  and O  $1s$  core level spectra from

**Table 6.8:** Average thickness of the oxide estimated from the FWHM of the  $(4, 0, 1)_M$  and  $(4, 0, \bar{1})_M$  oxide peaks after oxidation at (left) 600°C and (right) 650°C.

Peak	$L$	FWHM	Thickness	Peak	$L$	FWHM	Thickness
	(r.l.u.)	(r.l.u.)	(nm)		(r.l.u.)	(r.l.u.)	(nm)
$(4, 0, \bar{1})_M$	0.85	0.0326	9.0	$(4, 0, \bar{1})_M$	0.85	0.0243	12.0
$(4, 0, 1)_M$	1.08	0.0357	8.3	$(4, 0, 1)_M$	1.08	0.0258	11.2

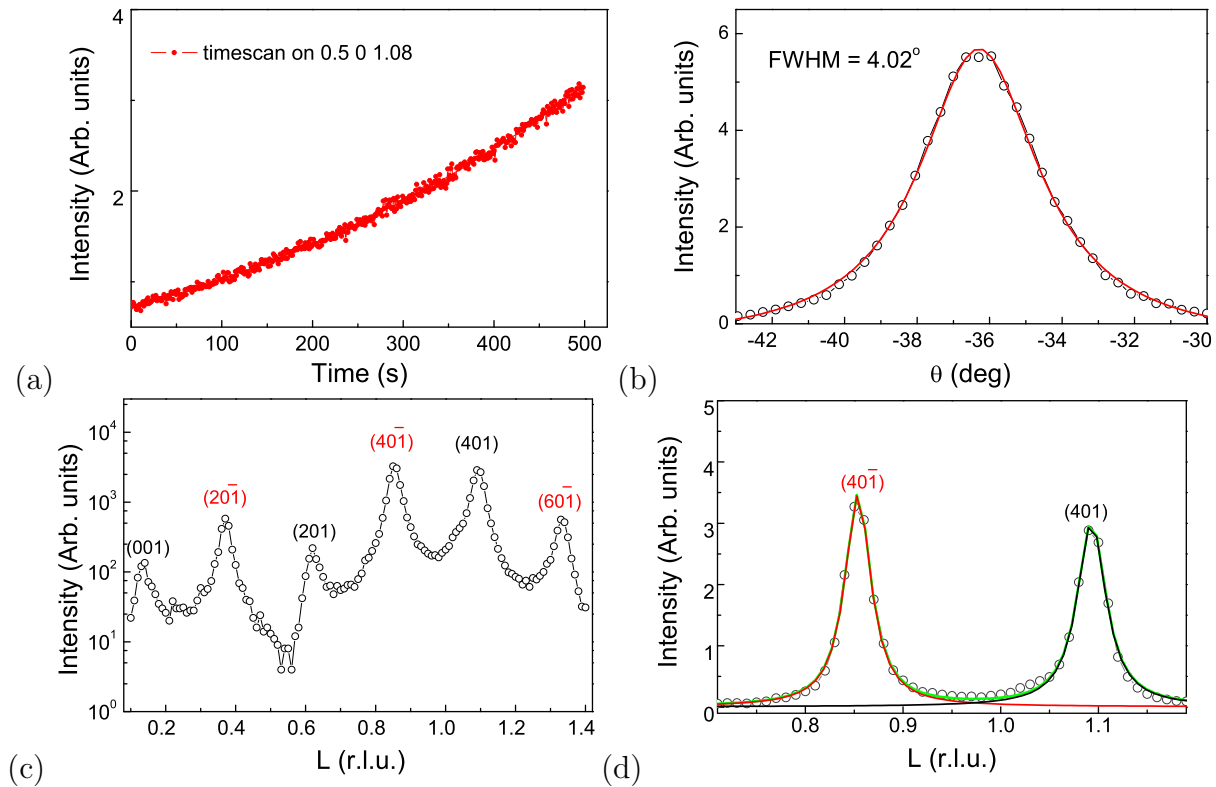


**Figure 6.22:** (a) Timescan on the  $(0.5, 0, 1.08)$  oxide peak during oxidation at  $600^\circ\text{C}$  and  $5 \times 10^{-2}$  mbar  $\text{O}_2$ . (b) Rocking scan on the  $(0.5, 0, 1.08)$  oxide peak. (c) Diffracted intensity along the  $(0.50L)$  reciprocal lattice direction. (d) Lorentz fit for the  $(4, 0, 1)_M$  and  $(4, 0, \bar{1})_M$  oxide peaks.

the surface oxide formed at  $450^\circ\text{C}$  and 5000 L oxygen (100 seconds at  $5 \times 10^{-5}$  mbar  $\text{O}_2$ ). The vertical dotted lines mark the binding energies of the components arising from the different Ga and O ions in the surface oxide.

Increasing the oxidation temperature to  $700^\circ\text{C}$ , a new Ga  $3d$  component emerges at higher binding energies, as can be seen in the middle panel in Fig. 6.25(a). The Ga  $3d$  component developing at higher binding energy can be understood in terms of Ga ions having a higher oxygen coordination and is consistent with the formation of a bulk-like gallium oxide. As the oxygen exposure and the temperature are raised to 25000 L (500 seconds at  $5 \times 10^{-5}$  mbar  $\text{O}_2$ ) and  $750^\circ\text{C}$ , respectively, this component increases in intensity, in conjunction with a strong decrease of the Ga  $3d$  bulk component (18.5 eV). A similar behavior is observed in the corresponding O  $1s$  spectra [Fig. 6.25(b), middle and bottom panel]: a higher binding energy component develops ( $\sim 532$  eV) and becomes more intense after oxidation at  $750^\circ\text{C}$ . From the relative intensity between the substrate Ga  $3d$  component ( $\sim 18.5$  eV) and the oxygen-induced components (high binding energy) it can be concluded that the oxide grown at  $750^\circ\text{C}$  with 25000 L  $\text{O}_2$  has a much higher thickness than the gallium oxide layers formed at  $T < 700^\circ\text{C}$ . The SXRD measurements

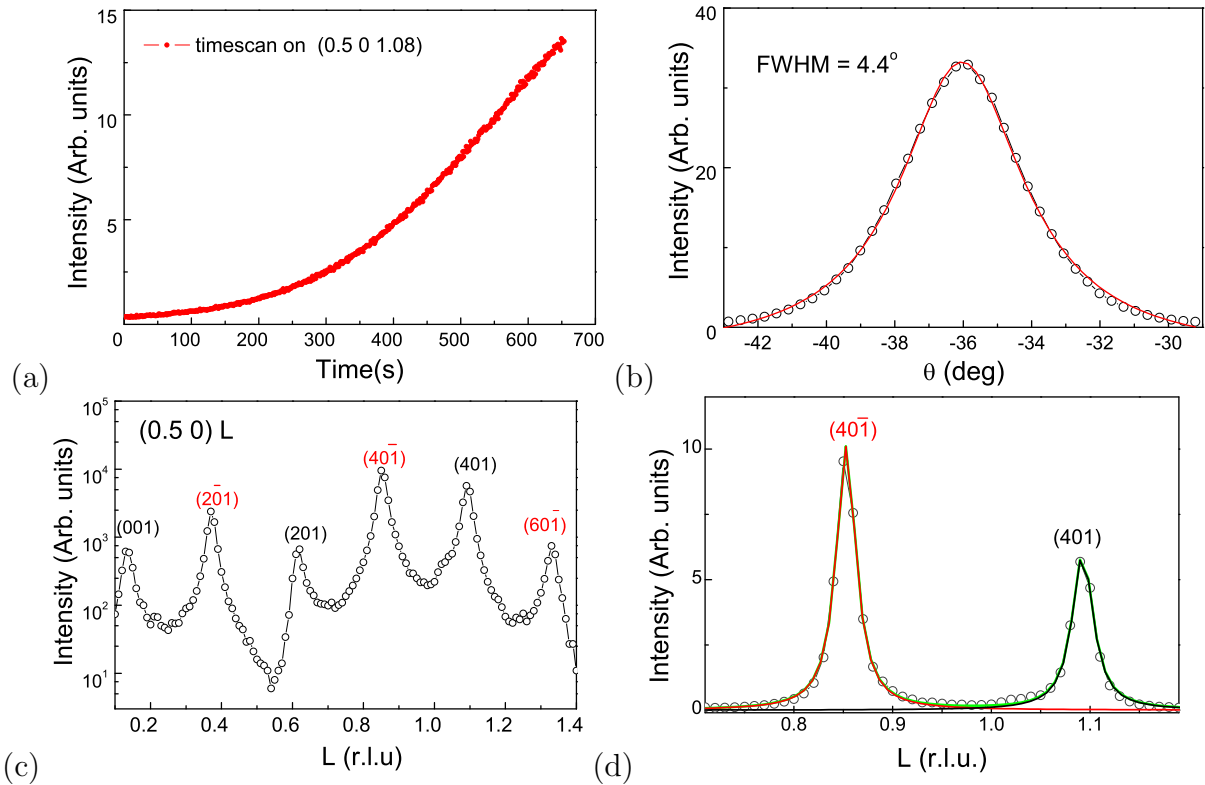


**Figure 6.23:** (a) Timescan on the (0.5, 0, 1.08) oxide peak during oxidation at 650°C and  $10^{-2}$  mbar  $O_2$ . (b) Rocking scan on the (0.5, 0, 1.08) oxide peak. (c) Diffracted intensity along the  $(0.50L)$  reciprocal lattice direction. (d) Lorentz fit the for  $(4, 0, 1)_M$  and  $(4, 0, \bar{1})_M$  oxide peaks.

confirmed the bulk  $\beta\text{-Ga}_2\text{O}_3$  oxide formation. Fig. 6.26(a)  $(00.5L)$  superstructure rod from the gallium oxide layer formed at 770°C and  $2.5 \times 10^{-5}$  mbar  $O_2$ . All the peaks present could be identified with the bulk  $\beta\text{-Ga}_2\text{O}_3$  reflections and have been labeled within the monoclinic coordinates. A rocking scan through the  $(4, 0, 1)_M$  oxide peak is plotted in Fig. 6.26(b). The FWHM was found to be comparable with the values obtained for the bulk oxide layers grown at different temperatures.

### Surface morphology

LEED patterns of the bulk oxide grown at 700 and 750°C revealed additional spots apart from the  $(2 \times 1)$  and  $(1 \times 2)$  superstructure reflections. The extra spots were found to move outwards with increasing electron energy. It is known that with the normal incidence of the primary electron beam, the  $(0, 0)$  specular spot will be located in the center of the screen. Increasing the electron energy will cause all the other diffraction spots to move continuously towards the  $(0, 0)$  spot, whose position remain fixed. The outward-moving diffraction spots observed in our measurements can be explained by surface faceting: if a plane is inclined by a certain angle different than  $90^\circ$  to the direction of the incident

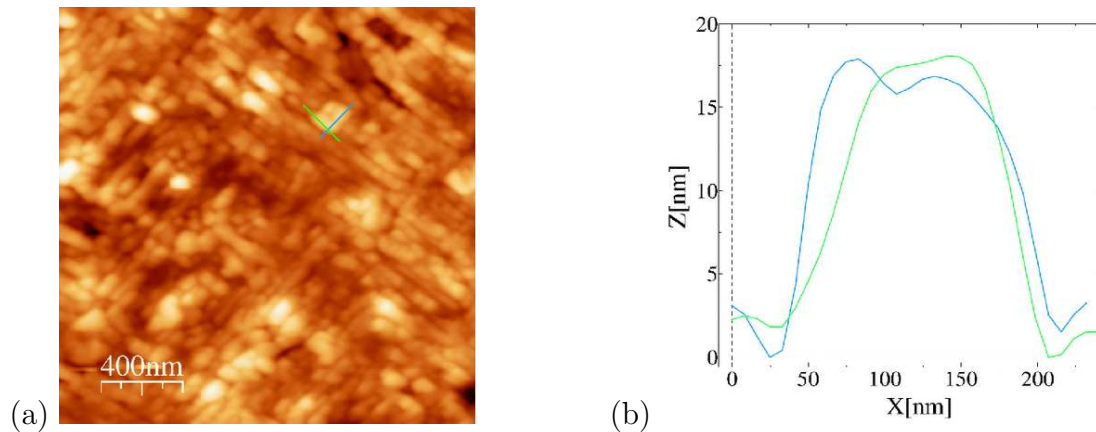


**Figure 6.24:** (a) AFM image showing the morphology of  $\beta$ -Ga<sub>2</sub>O<sub>3</sub>/CoGa(100) system after oxidation at 650°C. (b) Line profiles along the directions indicated in Fig. 6.24(a).

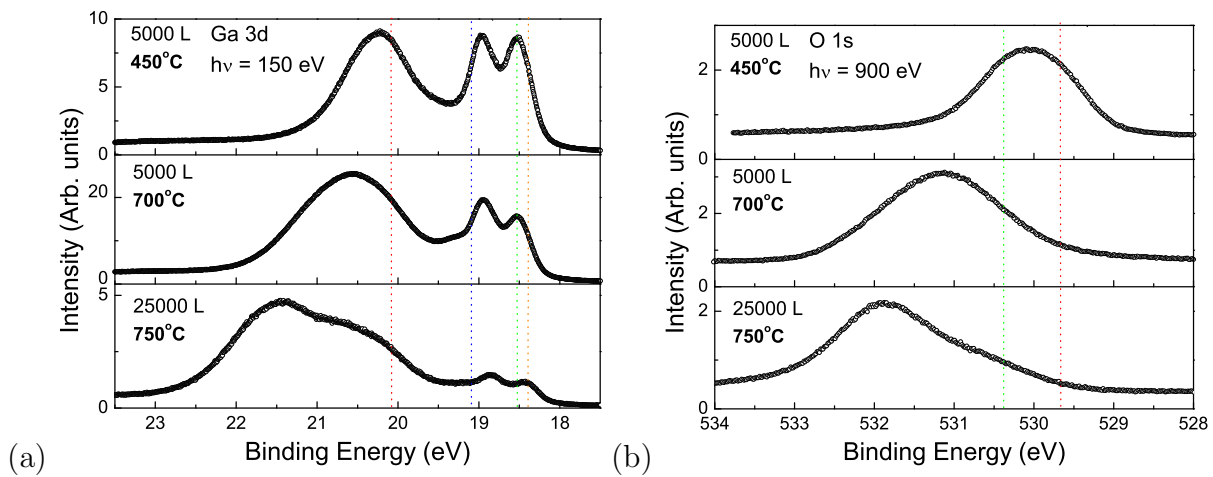


**Figure 6.25:** (a) Ga 3d and (b) O 1s spectra measured after oxidation at 700 and 750°C.

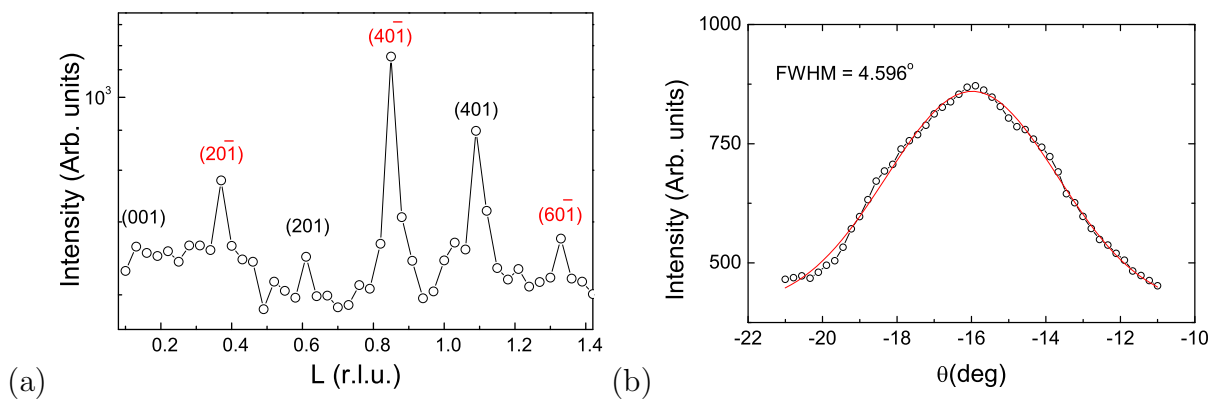


**Figure 6.26:** (a) Diffracted intensity along the  $(00.5L)$  reciprocal lattice direction after oxidation at 770°C and  $2.5 \times 10^{-5}$  mbar O<sub>2</sub>. (b) Rocking scan on the  $(0, 0.5, 1.08)$  oxide peak.

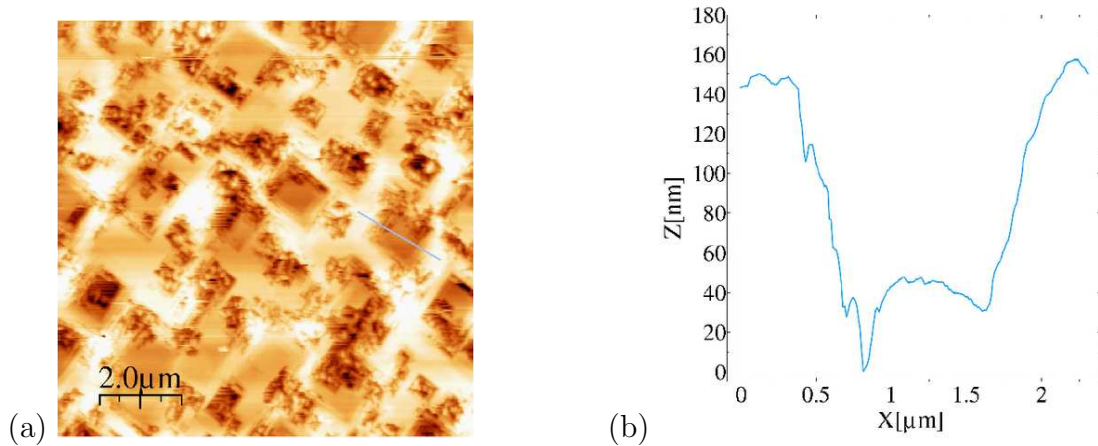


**Figure 6.27:** (a) AFM image ( $10 \times 10 \mu\text{m}^2$ ) of a  $\beta\text{-Ga}_2\text{O}_3$  on CoGa(100) grown after oxidation at  $770^\circ\text{C}$ . (b) Line profile of (a).

beam, the corresponding specular beam will be at a different position of the diffraction pattern. Therefore, with increasing the electron energy the diffraction spots from the facet surface will move continuously towards the corresponding specular spot. *Ex situ* AFM measurements have confirmed the facets formation on the oxide surface. The AFM images shown in Fig. 6.27(a) and (c) have been measured after oxidizing the sample 25000 L ( $5 \times 10^{-5}$  mbar  $\text{O}_2$  for 500 seconds) at  $750^\circ\text{C}$ . The oxide islands have been observed to form large rectangular-shaped cavities, like the one shown in Fig. 6.27(a) characterized by  $\sim 1 \mu\text{m}$  width and  $\sim 100$  nm height. The rectangular shape of the cavities is a consequence of the preferential growth of the oxide islands along two directions perpendicular to each other ([100] and [010] substrate directions).

### Substrate faceting

While the LEED and AFM measurements are suitable to investigate the oxide morphology and surface faceting, SXRD measurements have been performed to investigate the evolution of the oxide/substrate interface under the above mentioned oxidation conditions.

Fig. 6.28(a) shows  $H$ -scans parallel to the (100) substrate directions at  $K=1$  for different  $L$  values. Apart from the  $(01L)$  crystal truncation rod signal, additional rods which are not constant in  $H$  with increasing  $L$  value are observed as shoulders on both sides of the CTR. This is a direct proof for the facet formation, since any facet gives rise to a crystal truncation rod signal perpendicular to its surface.

In order to determine the angle between the (001) CoGa plane and the newly formed facets, each of the  $H$ -scans in the Fig. 6.28(a) was fitted and the position of the side maxima was accurately determined. These are plotted in Fig. 6.28(b) as black squares. A linear fit through the data points corresponding to each of the two facets allowed the

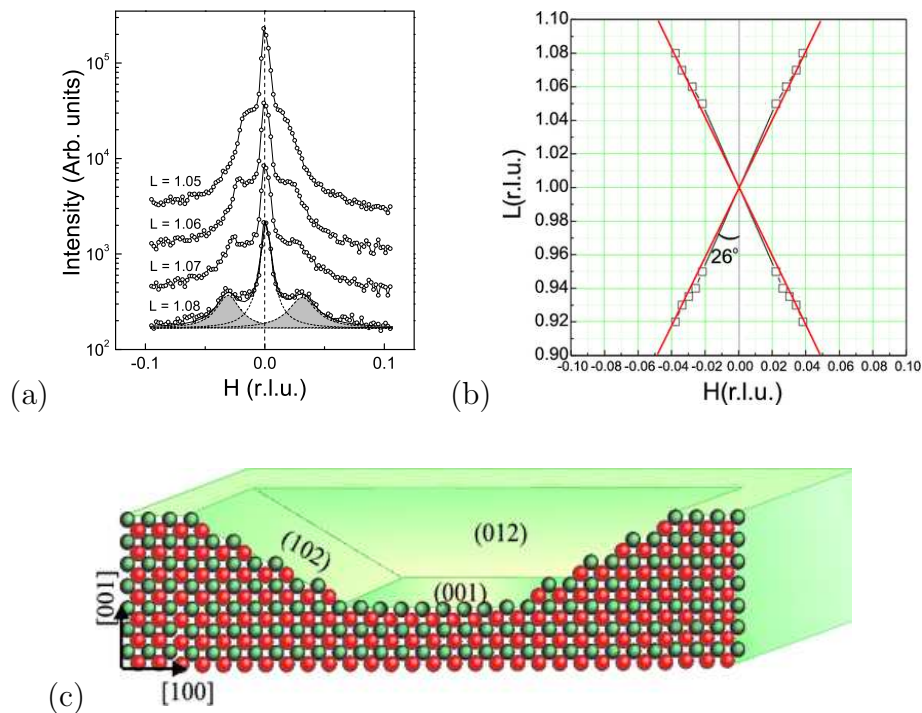


**Figure 6.28:** (a) Mesh scan around the (0, 1, 1) Bragg peak of CoGa. (b) The position of the side maxima as obtained from the fit of the line scans in (a). (c) A schematic representation of the (001)/{102} planes of the CoGa viewed along the  $[010]$  direction.

angle between the substrate surface and the facets to be determined. The angle was found to be  $26^\circ$ , corresponding to the (102) and  $(\bar{1}02)$ -type of facets. The presence of (012) and  $(0\bar{1}2)$  facets ( $\pm 90^\circ$  rotated with respect to the (102) facets) was evidenced by performing scans in the  $K$  direction (not shown) at  $H=0$  at different  $L$  values around the (011) substrate Bragg peak. A schematic representation of the (001)/{102} planes of the CoGa viewed along the  $[010]$  direction is shown in Fig. 6.28 (c). The {102}-type of planes consist of three atoms wide (101) terraces separated by monoatomic steps approximately 10 Å apart.

The presence of (012) and  $(0\bar{1}2)$  facets ( $\pm 90^\circ$  rotated with respect to the (102) facets) was evidenced by performing  $K$ -scans at  $H=0$  for different  $L$  values around the (0, 1, 1) substrate Bragg peak. As an example, in Fig. 6.29 (a) and (b) a  $K$ -scan at  $L=1.08$  and  $H=0$  and a  $H$ -scan at the same  $L$  value and  $K=1$  are shown, respectively. Three Lorentz functions were used to fit the main features of these scans: the central peak (red) represents the CTR signal arising from the original (001) surface and the side peaks (green) are indicative of the CTR signal of the facets. The average domain size of the four type of facets observed has been estimated from the FWHM of the facet peaks. The results are summarized in the Table 6.9. An additional peak (grey) had to be introduced when fitting the  $K$ -scan in the Fig. 6.29(a) due to the intersection with the (0, 1, 1) Debye-Scherrer

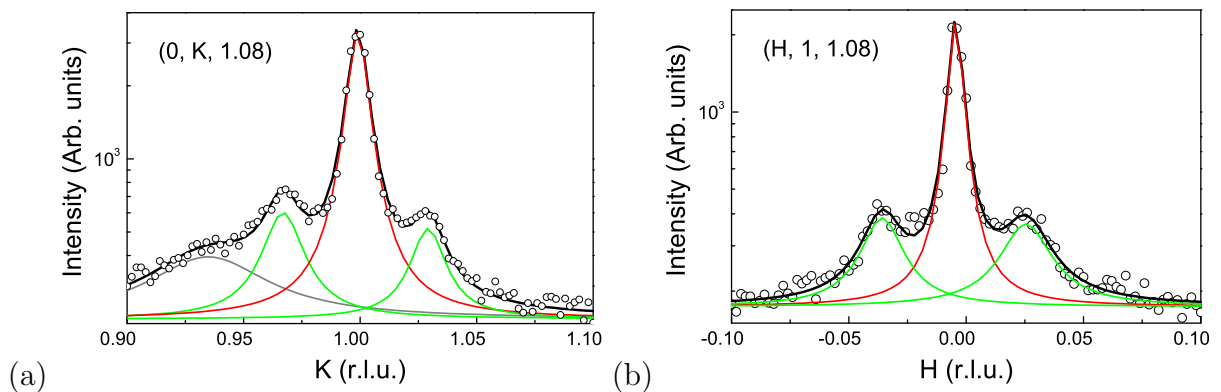
**Table 6.9:** Average size of the facets estimated from the FWHM of the measured peaks shown in Fig. 6.29.

Peak	FWHM ( $\text{\AA}^{-1}$ )	Average size ( $\text{\AA}$ )	Facet type
(0.03, 1, 1.08)	0.04	150	( $\bar{1}02$ )
( $0\bar{0}3$ , 1, 1.08)	0.05	125	(102)
(0, 1.03, 1.08)	0.035	180	( $0\bar{1}2$ )
(0, 0.97, 1.08)	0.04	150	(012)

ring of the substrate.

## 6.4 Summary

This chapter presented a study on the stability of the surface gallium oxide grown on CoGa(100) and its transition to bulk  $\text{Ga}_2\text{O}_3$  as a function of the oxidation conditions, namely the temperature and partial oxygen pressure. Structural information have been obtained by means of *in situ* surface x-ray diffraction performed at the MF-MPI beamline at the synchrotron radiation facility ANKA in Karlsruhe. High resolution core level spectroscopy and low energy electron diffraction measurements have been employed to study the CoGa(100) oxidation behavior at different temperatures up to  $750^\circ\text{C}$  and partial oxygen pressures ranging from  $10^{-8}$  to  $5 \times 10^{-5}$  mbar  $\text{O}_2$ . These measurements have been performed at the beamline I 311 at the Max-lab II, Sweden. Additional information on the surface morphology were obtained by means of *ex situ* AFM investigations. The main

**Figure 6.29:** Decomposition of line scans performed along the (a)  $K$  and (b)  $H$  directions at  $L=1.08$ . The contribution from the facets is given by the side peaks (green curves), whereas the middle peak represents the CTR signal (red curve).

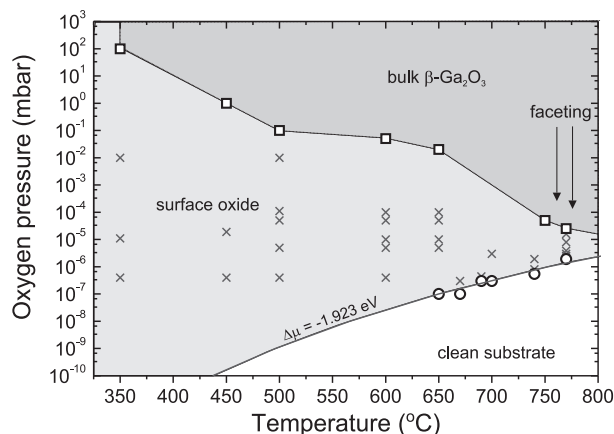


**Figure 6.30:** Experimental stability diagram of gallium oxide on CoGa(100).

experimental findings are summarized in the following:

### Surface gallium oxide structure

Using a multi-method approach, an atomic level understanding of the well-ordered surface gallium oxide structure has been achieved. The proposed structural model contains the basic building block of  $\beta$ -Ga<sub>2</sub>O<sub>3</sub>, but shows deviations from the bulk oxide stoichiometry. The oxide film consists of an oxygen ion double layer with two Ga ions located in truncated octahedral and tetrahedral sites of the fcc oxygen ion sublattice. At the interface, the Ga ions occupy sites of the corresponding stacking sequence of the bulk  $\beta$ -Ga<sub>2</sub>O<sub>3</sub>. The two oxygen interfacial atoms share half of their bonds with the strongly buckled Ga substrate atoms, recovering the formal oxidation state of Ga<sup>3+</sup> in the oxide film. The thickness of the surface gallium oxide film is about 4.5 Å.

An excellent agreement between the SXR D data and the DFT-based calculations has been achieved. In addition, the comparison between the calculated core level shifts and the deconvoluted HRCLS experimental spectra brought an additional evidence which supports the proposed structural model.

### Experimental stability diagram of gallium oxide on CoGa(100)

The stability diagram of the gallium oxide formation on CoGa(100) at different temperatures up to 770°C was mapped out by means of *in situ* SXR D measurements. Throughout the investigated ( $p$ - $T$ ) range, either the surface oxide or  $\beta$ -Ga<sub>2</sub>O<sub>3</sub> bulk oxide was found to form. The stability conditions for surface or bulk gallium oxide at different temperatures and partial oxide pressures as observed experimentally are indicated in Fig. 6.30. The white area marks the regime where the clean substrate is stable, whereas the light and the dark grey areas correspond to the surface and bulk gallium oxide stability region, respectively.

Depending on the temperature, the surface gallium oxide was found to form at oxy-

gen pressures between  $10^{-7}$  and  $2.6 \times 10^{-6}$ , as indicated in Fig. 6.30. During oxidation at  $670^\circ\text{C}$  and  $3 \times 10^{-7}$  mbar  $\text{O}_2$ , a very rapid initial oxide growth was observed [97]. However, decreasing the oxygen pressure to  $10^{-7}$  mbar caused the intensity to drop down, revealing the instability of the oxide at lower oxygen pressures. The bulk oxide formation is kinetically hindered at  $T < 350^\circ\text{C}$ , the surface gallium oxide being stable at room temperature even at 1 bar oxygen. At temperatures higher than  $450^\circ\text{C}$  and when enough oxygen is supplied to the system, three-dimensional bulk  $\text{Ga}_2\text{O}_3$  islands form epitaxially on  $\text{CoGa}(100)$ . The same surface termination as the ultra-thin gallium oxide layer was identified for the bulk oxide formed at 600 and  $650^\circ\text{C}$ . The average thickness of the bulk gallium oxide is increasing with increasing the oxidation temperature, as shown in Fig. 6.31.

The temperature,  $T$ , and partial oxygen pressure,  $p$ , are known to be directly related to the chemical potential of oxygen,  $\mu_{\text{O}}(T, p)$ , as shown in the expression below:

$$\mu_{\text{O}}(T, p) = \frac{1}{2}E_{\text{O}_2}^{\text{tot}} + \mu_{\text{O}}(T, p^0) + \frac{1}{2}k_{\text{B}}T \ln(p/p^0), \quad (6.2)$$

where  $k_{\text{B}}$  is the Boltzmann constant and  $p^0=1$  bar is the standard pressure [39]. Accurate values of the oxygen chemical potential at the reference pressure  $p^0$ ,  $\mu_{\text{O}}(T, p^0)$ , at different temperatures are available in thermochemical tables [99]. The above formula allows to convert our experimental results obtained in terms of partial oxygen pressure at specific temperature into oxygen chemical potential. The total energy of an oxygen molecule in the gas phase,  $E_{\text{O}_2}^{\text{tot}}$ , is usually taken as a reference and one can write Eq. 6.3 as:

$$\Delta\mu_{\text{O}}(T, p) = \mu_{\text{O}}(T, p) - \frac{1}{2}E_{\text{O}_2}^{\text{tot}}, \quad (6.3)$$

where  $\Delta\mu_{\text{O}}(T, p)$  is defined as  $\mu_{\text{O}}(T, p) - \frac{1}{2}E_{\text{O}_2}^{\text{tot}}$ .

Based on the above relation and the experimental value of  $p$  corresponding to the surface oxide formation at  $650^\circ\text{C}$ , the chemical potential  $\Delta\mu_s$  was evaluated to be  $-1.92$  eV.

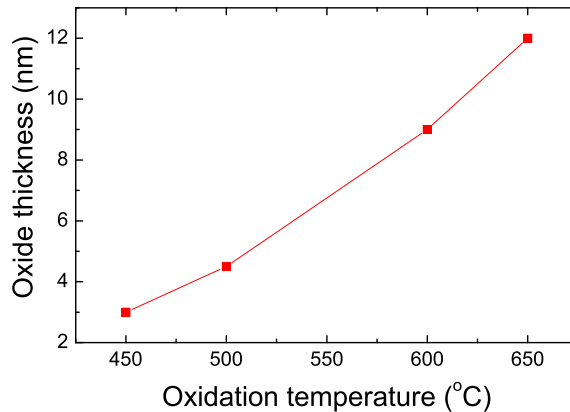


**Figure 6.31:** Evolution of the bulk gallium oxide thickness vs. the oxidation temperature.

This value was then considered for plotting the solid line separating the clean substrate and the surface gallium oxide stability range in Fig. 6.30. It is important to notice that the experimental points fall on this line of constant chemical potential, as expected for systems at equilibrium. However, this observation is inconclusive as to whether the surface oxide exist due to thermodynamics or its formation is kinetically driven.

Both SXRD and HRCLS investigations have shown that at temperatures higher than 750°C, the formation of a much thicker bulk oxide takes place. After oxidation at 750°C and  $5 \times 10^{-5}$  mbar O<sub>2</sub>, an additional component shifted to higher binding energy was observed both in Ga 3*d* and O 1*s* spectra. This might be an indication for the formation of a mixed Co and Ga oxide: different mixed oxides having the spinel structure have been reported to form on the surfaces of the Co-rich CoGa alloys [100].

The bulk oxide grown at temperatures higher than 750°C is accompanied by substrate faceting. The angle between the substrate and the facets was determined from the SXRD data to be 26°, which corresponds to the (102)-type of planes. The development of a similar substrate morphology was often observed after the high temperature oxidation of NiAl [101] and polycrystalline CoGa [100]. The formation of cavities is due to the selective oxidation of one component—in our case, Ga—which results in a supersaturation of vacancies at the metal-oxide interface. The condensation of these defects leads ultimately to cavity formation. According to Ref. [100], vacancies on the gallium sublattice, V<sub>Ga</sub>, develop due to the loss of gallium in the alloy surface. These vacancies are not stable and react with regular cobalt atoms, Co<sub>Co</sub>, to form a cobalt anti-site Co defect, Co<sub>Ga</sub>, and a cobalt vacancy, V<sub>Co</sub> on nearest neighbor sites:



If the supersaturation of defects near the surface is large enough, the formed voids may condense to macroscopic defects or cavities. Since the surface energy is structure dependent the shape of the cavities will reflect the crystallographic orientation of the initial alloy surface.